

Table of Contents

1	Excited State Quantum Cascade Lasers and High k-Space Lasing	2
1.1	The Long-wavelength Challenge	4
1.2	Excited State Transitions	6
1.3	Excited State QC Laser Design	10
1.4	Device Emission Characteristics	13
1.4.1	Electroluminescence & Transition Identification	13
1.4.2	Laser Emission	16
1.4.3	Stacked Transitions (?)	16
1.5	Anti-correlated Light Output Behavior	18
1.6	Lasing High in k -Space	22
1.7	Effects of Non-parabolicity	25
1.8	Rate Equation Modeling	28
1.8.1	A Dual-Optical Transition Coupled System	28
1.8.2	Comparing Threshold Data with Simulation	31
1.8.3	Cavity-length-dependence of Threshold Crossover	33
1.9	Conclusions & Future Directions	34
1.9.1	Summary	34
1.9.2	Future Direction: <i>Intentionally</i> create k -space lasers	36
1.9.3	Future Direction: Further develop the excited state concept	37
1.9.4	Future Direction: Correlated photons	37
	References	39

Excited State Quantum Cascade Lasers and High k -Space Lasing

The work-horse material system for mid-infrared QC lasers—InGaAs / AlInAs—has a limited range of wavelengths where the fundamental properties of the material system are most amenable to high performance QC designs. The lower end of this “sweet spot” is currently around 4.2 μm , as discussed in Chapter 2. And while the lower limit imposed by material band offsets is relatively abrupt, QC lasers experience gradual but steadily decreasing performance at longer wavelengths. Beyond 12 μm , performance is severely restrained: CW RT QC laser sources beyond 12 μm have not yet been demonstrated.

Indeed, the lack of high performance long-wavelength sources is a problem; a host of pressing applications are in critical need of such technology. For example, the strongest absorption lines for aromatic hydrocarbons are in the 12–16 μm range, as shown in Fig. 1.1 for BTEX (benzene, toluene, ethylbenzene, and xylenes) compounds. The ability to detect benzene, with a fundamental absorption at 14.8 μm , is of particular interest to the petro-chemical refining industry. Another immediate example is uranium hexafluoride (UF_6), a molecule that in its gas phase is a primary precursor in uranium enrichment processes [1]. UF_6 has isotopically-distinct absorption lines near 16 μm [2] [3].

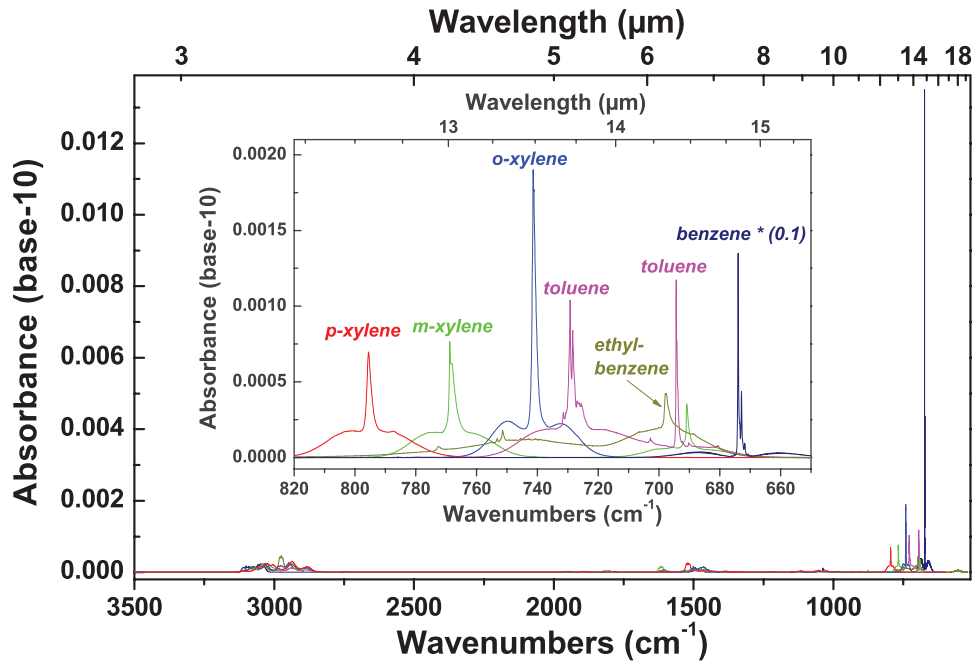


Figure 1.1: Absorption spectra for BTEX molecules. Compared with the fundamental vibrational absorption lines of most molecules, aromatic hydrocarbons have their strongest absorption lines at relatively long wavelengths. Benzene, for example, has an especially strong absorption at 14.8 μm . The absorption lines of BTEX compounds are spectrally distinct, providing an avenue for detection selectivity of these compounds.

The absence of RT CW QC laser sources with emission beyond 12 μm has not been for a lack of trying. Pushing QC capabilities to longer wavelengths began as early as 1998, when C. Gmachl *et al.* reported 13 μm emission from a convention single-phonon, three well active region QC structure [4]. This laser operated up to a pulsed $T_{\text{max}} \approx 175$ K. In 1999, A. Tredicucci *et al.* found the QC superlattice architecture well-suited for longer-wavelength emission, with the demonstration of lasing at 17 μm [5]. Superlattice structures later showed emission at 19 μm [6] and then 21.5 and 24 μm [7]. Each of these superlattice demonstrations exhibited a pulsed $T_{\text{max}} \approx 140$ K. Without question the best performance demonstrated by a long-wavelength QC laser was by M. Rochat *et al.* at 16 μm [8] [9]. For this “bound-to-continuum” structure, pulsed $T_{\text{max}} > 333$ K. Clearly, history has proven longer-wavelength light generation to be a substantial challenge.

In this chapter, I discuss a QC laser design strategy—namely the use of “excited state” optical transitions—intended to boost oscillator strength and thereby overcome many

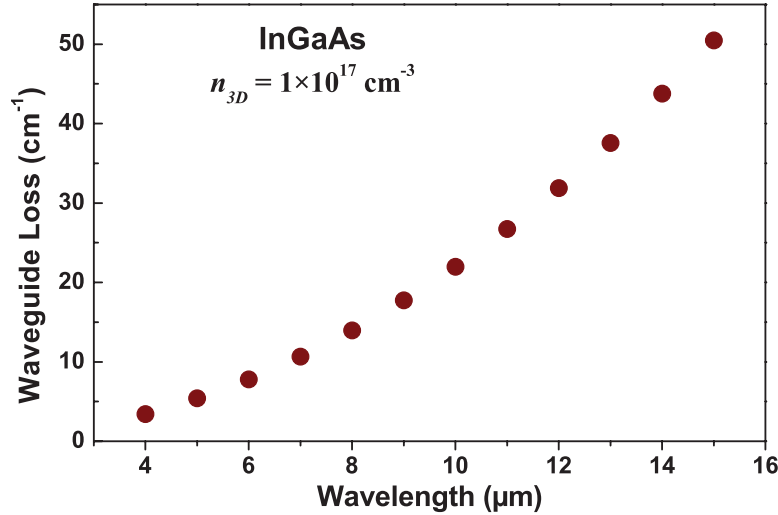


Figure 1.2: Optical absorption of bulk InGaAs. Calculated for $\text{In}_{0.53}\text{Ga}_{0.47}\text{As}$ with a free electron density $n_{3D} = 1.0 \times 10^{17} \text{ cm}^{-3}$. Waveguide loss increases super-linearly with wavelength.

of the aggravating factors preventing high performance lasing at longer wavelengths. While the excited state concept shows promise for such an effect, we discovered that these excited state QC structures are capable of simultaneous dual-wavelength lasing from two different optical transitions within the active region. Furthermore, the secondary emission shows some extra-ordinary properties. The interplay between charge carriers within the active region led to the secondary lasing transition being suppressed until a thermal turn-on; under certain circumstances, performance for the secondary emission actually *improves* with temperature. Ultimately, we found that the secondary emission is lasing only high in k -space: the lasing originates from electrons in a highly non-equilibrium state.

1.1 The Long-wavelength Challenge

The technical hurdles confronted in the pursuit of long-wavelength lasing are perhaps even more daunting than those imposed by material band offsets at the short wavelength limit. Two primary mechanisms—optical absorption loss and decreased upper laser state lifetimes—individually compound in a situation that frustrates QC designs and performance at longer wavelengths.

Optical absorption loss, or waveguide loss α_w , is related to the complex refractive index \tilde{n} as

$$\alpha_w = 2 \frac{2\pi \text{Im}[\tilde{n}]}{\lambda_0}. \quad (1.1)$$

In the long-wave infrared region, \tilde{n} is especially impacted by the presence of free carriers (i.e., electrons). For bulk materials, \tilde{n} can be estimated using the Drude model. Given a plasma frequency $\omega_p = \sqrt{\frac{4\pi q^2 n_{3D}}{m^* \epsilon_{inf}}}$, which is dependent on the free electron density n_{3D} and the electron effective mass m^* , the complex refractive index \tilde{n} is

$$\tilde{n} = \sqrt{\epsilon_\infty \left(1 - \frac{\omega_p^2}{\omega^2 + i\frac{\omega}{\tau}} \right)}. \quad (1.2)$$

A calculation for α_w in bulk $\text{In}_{0.53}\text{Ga}_{0.47}\text{As}$ for a typical doping $n_{3D} = 1 \times 10^{17} \text{ cm}^{-3}$ shows the dramatic increase of waveguide loss with wavelength. As shown in Fig. 1.2, while at $\lambda = 5 \mu\text{m}$ the waveguide loss $\alpha_w \approx 5 \text{ cm}^{-1}$, at $\lambda = 15 \mu\text{m}$, $\alpha_w \approx 50 \text{ cm}^{-1}$!

The ability to attain population inversion also becomes more difficult at longer wavelengths. A fundamental mechanism of most all QC lasers is the use of LO phonon scattering to rapidly depopulate the lower laser state. For a generic three level QC active region, as in Fig. 1.3b, one seeks to position the lowest two energy states one LO phonon energy apart ($\mathcal{E}_{21} \geq \hbar\omega_{LO}$); in InGaAs, $\hbar\omega_{LO} \approx 34 \text{ meV} \approx 36 \mu\text{m}$. As shown in Fig. 1.3a, the LO phonon scattering time for $\mathcal{E}_{21} = \hbar\omega_{LO}$ is about 0.2 ps. For the optical transition ($|3\rangle \rightarrow |2\rangle$) in Fig. 1.3b, the lifetime due to phonon scattering decreases as the transition energy decreases. However, as \mathcal{E}_{32} approaches \mathcal{E}_{21} , τ_{32} and τ_2 become similar. With population inversion (and therefore gain) proportional to $\left(1 - \frac{\tau_2}{\tau_{32}}\right)$, maintaining the ability to achieve population is most definitely a concern at longer wavelengths.

The combination of small photon energies, high waveguide losses, and short upper-state lifetimes make long-wavelength QC lasers fundamentally inefficient devices. From Chpt. 2, wall-plug efficiency

$$\eta_{WPE} = \left(\frac{\mathcal{E}_{ph}}{\mathcal{E}_{ph} + \Delta_{inj} + \frac{qR_{series}I}{N_p}} \right) \left(\frac{\alpha_m}{\alpha_w + \alpha_m} \right) \left(\frac{\tau_{eff}}{\tau_{eff} + \tau_2} \right) \left(\frac{J}{J - J_{th}} \right) \xi_{inj}. \quad (1.3)$$

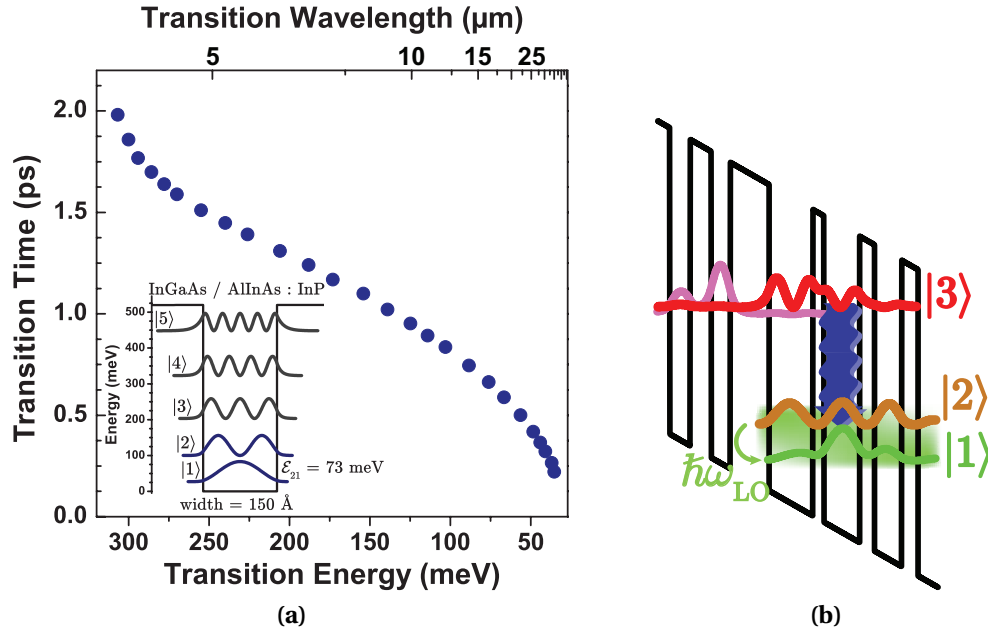


Figure 1.3: LO phonon lifetime vs. transition wavelength. (a) For a single quantum well, the LO phonon scattering time is plotted for decreasing $|2\rangle \rightarrow |1\rangle$ transition energy \mathcal{E}_{21} (increasing transition wavelength). For $\hbar\omega_{LO} < 34$ meV ≈ 36 μm, the small transition energy precludes scattering by LO phonons, the fastest scattering process in semiconductors. (b) A schematic representation of a conventional single-phonon active region with optical transition $|3\rangle \rightarrow |2\rangle$ and phonon transition $|2\rangle \rightarrow |1\rangle$.

The implications of long-wavelength lasing affect nearly every component term that contributes to the overall wall-plug efficiency. The small photon energy \mathcal{E}_{ph} relative to the fixed values of Δ_{inj} and R_{series} substantially reduce voltage efficiency. And while high waveguide losses hurt the out-coupling efficiency, they also decrease current efficiency by increasing J_{th} . Likewise, the short upper-state lifetimes increase J_{th} and decrease current efficiency, in addition to decreasing transition efficiency term.

1.2 Excited State Transitions

A chief battle long-wavelength lasers must overcome is simply “turning on”—i.e., reaching threshold—at a current density below J_{max} . The challenges posed by long-wavelength lasing are in large part fundamental; the effects of free carrier absorption and phonon lifetimes are built-in properties of the system. However, many design parameters

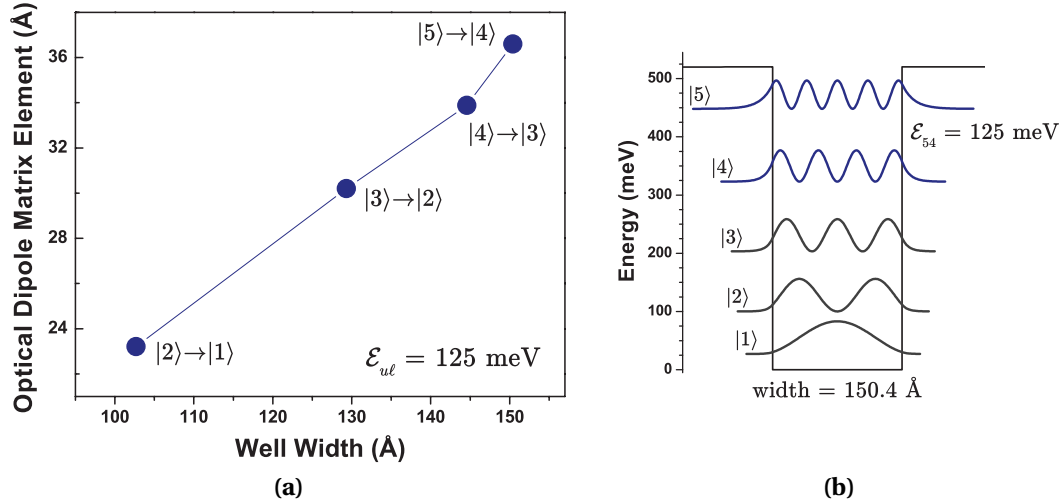


Figure 1.4: Optical dipole matrix elements for a single quantum well. (a) The calculated optical dipole matrix element of the specified transition, where well width has been adjusted to give a transition energy $\mathcal{E}_{ul} = 125$ meV. For this constant transition energy, the optical dipole matrix elements and quantum well widths increase for transitions between higher lying adjacent levels. Here we simulate optical transitions in the InGaAs/AlInAs:InP system, which has a conduction band offset of 520 meV. (b) An example configuration for the single quantum well calculation, where the $|5\rangle \rightarrow |4\rangle$ transition energy $\mathcal{E}_{54} = 125$ meV at a well width of 150.4 Å.

affected by the QC quantum design itself are included in threshold current density:

$$J_{th}(T=0) = \frac{\alpha_m + \alpha_w}{g\Gamma} \quad (1.4)$$

where

$$g = \frac{4\pi q}{\lambda_0 \epsilon_0 n_{eff}} \frac{1}{\delta \mathcal{E}_{ul}} \frac{\tau_u (1 - \tau_\ell / \tau_{ul}) z_{ul}^2}{L_p}. \quad (1.5)$$

If optical losses and phonon scattering times cannot be directly affected by clever design, another strategy might be to compensate for these effects by boosting the values of other parameters. For example, the optical dipole matrix element z_{ul} contributes quadratically to gain. Thus, a modest increase in z_{ul} can have a rather substantial overall impact on lowering J_{th} .

The optical dipole matrix element between two energy states z_{ul} can be simplistically thought of as the amount of spatial overlap between those states: the more overlap, the larger is z_{ul} . Using the example of a single quantum well, as in Fig. 1.4,

it is interesting to observe the relation between various consecutive energy states and $z_{u\ell}$. By keeping the transition energy constant—in this case $\mathcal{E}_{u\ell} = 125$ meV—we get a fair comparison of $z_{u\ell}$ for the ladder of adjacent energy states in the well. Clearly, $z_{u\ell}$ increases for higher-lying transitions. In this example, $z_{21} = 23.2$ Å and $z_{32} = 30.2$ Å, suggesting a potential increase in gain by a factor of 1.7 (considering the quadratic contribution to optical gain) when using a $|3\rangle \rightarrow |2\rangle$ optical transition rather than a $|2\rangle \rightarrow |1\rangle$ transition.

Further examination of Fig. 1.4a suggests another benefit from using excited state transitions. To keep the transition energy constant while climbing the ladder of transitions between adjacent states, the well itself must be widened. Intuitively, wider wells mean that a relatively smaller portion of the upper laser state wavefunction is perturbed by inhomogeneity at well–barrier interfaces. In most QC lasers, interface roughness-induced broadening is the dominant contributor to the gain spectrum width $\delta\mathcal{E}_{u\ell}$ [10]. With J_{th} being proportional to $\delta\mathcal{E}_{u\ell}$, wider QC active region quantum wells can be expected to be a net benefit for laser performance.

By this logic, making use of “excited state” transitions—those made purely from quantum mechanical excited states—is a potential approach for increasing QC laser gain and decreasing threshold current densities. Yet with the multitude of coupled quantum wells that make up a QC laser design, it may not be immediately clear what an excited state QC laser might look like. In the case of the single quantum well in Fig. 1.4, identifying excited states is quite simple: the lowest energy state in the well is the ground state, and each state above the ground state is an excited state. Thus, any transition not between $|2\rangle \rightarrow |1\rangle$ is an excited state transition.

In the case of coupled quantum wells, what particularly matters for our characterization of excited state transitions is more the “shape” of the energy state, rather than an individual state’s position relative to the other states in the system. A pictorial example may be helpful. In Fig. 1.5, we have three coupled quantum wells; Fig. 1.5a plots our usual $\langle\psi(z)|\psi(z)\rangle$ while Fig. 1.5b plots $\psi(z)$. As in our example of a single quantum well, each of the coupled quantum wells will contribute to the system an energy state that looks quantum mechanically like a ground state; that is, each coupled well contributes to the system one state with a shape having zero nodes within each coupled well. Momentarily ignoring the narrow well A, the states labeled $|1\rangle$ and $|2\rangle$ are the “ground

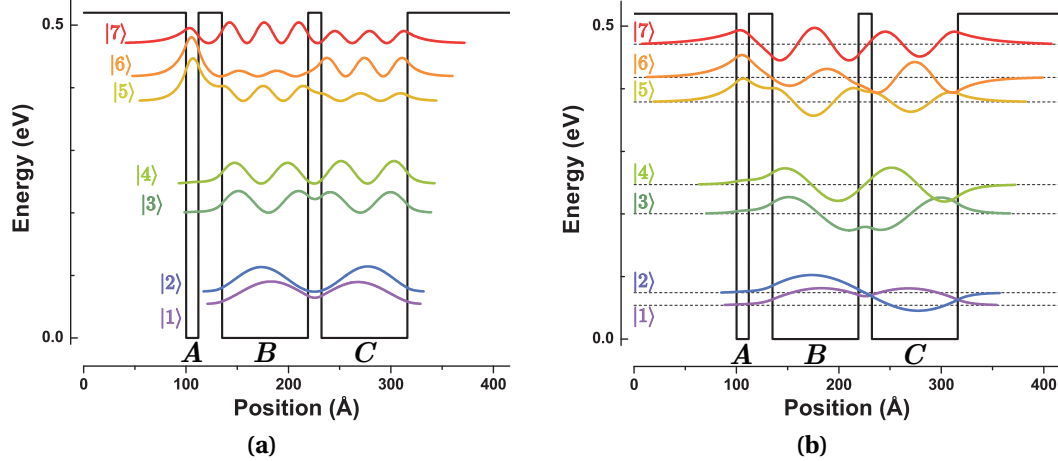


Figure 1.5: Energy state mixing in coupled quantum wells. A pictorial example of energy state mixing calculated for a three coupled quantum well $\text{In}_{0.53}\text{Ga}_{0.47}\text{As} / \text{Al}_{0.48}\text{In}_{0.52}\text{As}$ system. The quantity $\langle \psi(z) | \psi(z) \rangle$ is plotted in (a) and $\psi(z)$ is plotted in (b). States |1> and |2> are ground states, and |3> and |4> are first-excited states. States |5>, |6>, and |7> are largely second-excited states, with some ground state character in well A.

states” for the coupled wells B and C. Likewise, each coupled well will contribute one first-excited state; the states labeled |3> and |4> are “first-excited states” for the coupled wells B and C, since they each have one node within each coupled quantum well. The characterization gets a notch more complicated when narrow wells are placed adjacent to wide wells (as in the case of a QC laser with the conventional narrow injector well adjacent to the first wide active region well). This creates a situation where a ground state “mixes” with an excited state, such as the case for states |5>, |6>, and |7>. Each state in this group has zero nodes in well A, but two nodes in wells B and C; over most of their probability densities, |5>, |6>, and |7> are characteristically second-excited states, with some ground state shape in well A.

Using this convention, most all QC lasers to date have used a first-excited state and ground state, respectively, for the upper and lower states of the laser transition. For example, the now classical double-phonon design * [11] uses three wide active region wells, thus yielding three ground states |3>, |2>, and |1>—with \mathcal{E}_{32} and \mathcal{E}_{21} roughly the energy of one LO phonon. The upper laser state, conventionally labeled |4>, is a first-excited state, making the laser transition |4>→|3> a first-excited state to ground state

* For an example conventional double phonon band structure, see Fig. ??.

transition. There are, however, a few examples in the literature of QC lasers that have used optical transitions composed completely from excited states. In an attempt to achieve a “cascaded” QC laser—that is, a QC active region with sequentially stacked optical transitions that would be a scheme for correlated photon generation [12]—J. Faist *et al.* injected electrons into state $|3\rangle$ of a single quantum well active region. In this work, they observed lasing from $|3\rangle \rightarrow |2\rangle$, an excited state transition similar to $|3\rangle \rightarrow |2\rangle$ in Fig. 1.4b. Notably, they were unable to achieve lasing from $|2\rangle \rightarrow |1\rangle$. More examples exist for THz QC lasers—lasers where $\hbar\omega_{ph} < \hbar\omega_{LO}$. In a THz QC structure, G. Scalari *et al.* also observed stacked transitions; in this case different applied electric field values resulted in switching emission between $|3\rangle \rightarrow |2\rangle$ and $|4\rangle \rightarrow |3\rangle$, yielding field-selectable output at either $\mathcal{E}_{32} = 5.75$ meV (1.39 THz) or $\mathcal{E}_{43} = 9.5$ meV (2.3 THz).

1.3 Excited State QC Laser Design

We have implemented an excited state QC laser design in a two-well active region configuration using $\text{In}_{0.53}\text{Ga}_{0.47}\text{As}$ wells and $\text{Al}_{0.48}\text{In}_{0.52}\text{As}$ barriers. The conduction band energy diagram is shown in Fig. 1.6. Rather than injecting electrons into state $|3\rangle$ as in a conventional two-well (single-phonon) QC laser, our injector region is specifically designed on the downstream side to inject electrons into state $|5\rangle$. Our optical transition is thus designed to be between states $|5\rangle$ and $|4\rangle$; because $|5\rangle$ is a second-excited state and $|4\rangle$ is a first-excited state, the transition $|5\rangle \rightarrow |4\rangle$ is an excited state transition. The design energy $\mathcal{E}_{54} = 128$ meV ($\lambda = 9.68$ μm). The injector region is also designed with relatively narrow barriers on the upstream side; these narrow barriers result in a large splitting of the injector states, intended to efficiently empty out the active region states $|4\rangle$ through $|1\rangle$.

The laser was grown using gas-source molecular beam epitaxy on a low-doped ($n_{3D} < 2 \times 10^{17} \text{ cm}^{-3}$) InP:S substrate. The active core consisted of 40 active–injector region periods, and the design included 0.55 μm of $\text{In}_{0.53}\text{Ga}_{0.47}\text{As}$ (Si-doped $n_{3D} = 5 \times 10^{16} \text{ cm}^{-3}$) for the cladding regions above and below the QC stack. A 0.9 μm InP ($n_{3D} = 5 \times 10^{16} \text{ cm}^{-3}$) buffer layer was grown before the bottom $\text{In}_{0.53}\text{Ga}_{0.47}\text{As}$ cladding. After the top $\text{In}_{0.53}\text{Ga}_{0.47}\text{As}$ cladding, additional cladding layers of 3.9 μm InP ($n_{3D} = 5 \times 10^{16} \text{ cm}^{-3}$) and 1.1 μm

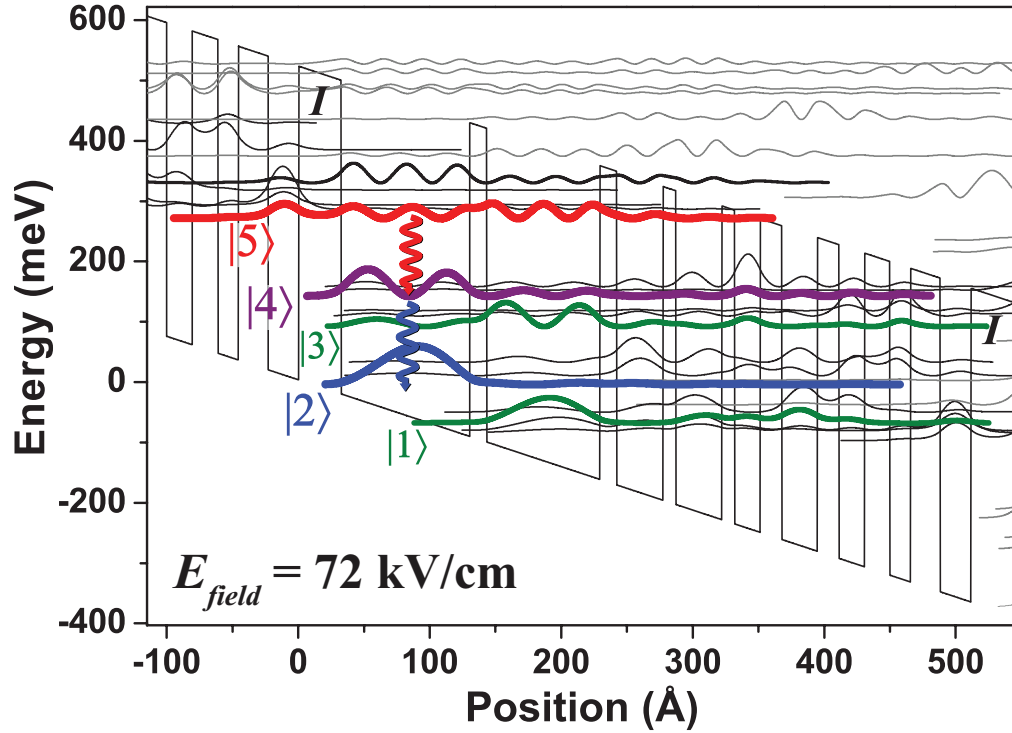


Figure 1.6: Excited state QC laser band diagram. Optical transitions are observed between states $|5\rangle \rightarrow |4\rangle$ and $|4\rangle \rightarrow |2\rangle$.

InP ($n_{3D} = 6.7 \times 10^{18} \text{ cm}^{-3}$) were grown, before capping the growth with $0.06 \mu\text{m}$ of $\text{In}_{0.53}\text{Ga}_{0.47}\text{As}$ ($n_{3D} = 2 \times 10^{19} \text{ cm}^{-3}$).

The as-grown structure, plotted in the Fig. 1.6 conduction band diagram is, in angstroms from the injection barrier, **32.3** / 97.7 / **12.9** / 86.0 / **12.9** / 35.2 / **9.7** / 35.2 / **9.7** / 19.5 / **16.1** / 27.4 / **16.1** / 19.5 / **19.4** / 15.6 / **22.6** / 23.5. Here, $\text{Al}_{0.48}\text{In}_{0.52}\text{As}$ layers are in bold type, $\text{In}_{0.53}\text{Ga}_{0.47}\text{As}$ layers are in plain type, and layers Si-doped $n_{3D} = 2 \times 10^{16} \text{ cm}^{-3}$ are underlined; the structure has an active core sheet density $n_s = 1.6 \times 10^{11} \text{ cm}^{-2}$.

Following growth, we post-calibrated our structure by measuring active region and cladding layer thicknesses with high magnification scanning electron microscope (SEM) images, such as in Fig. 1.7. Here, we are able to see each individual QC period in the active core, along with the $\text{In}_{0.53}\text{Ga}_{0.47}\text{As}$ cladding layers, giving us an accurate measurement of the actual period thicknesses. $\text{In}_{0.53}\text{Ga}_{0.47}\text{As}$ cladding thicknesses showed the $\text{In}_{0.53}\text{Ga}_{0.47}\text{As}$ growth rate was slow by a factor of 0.96 from the original

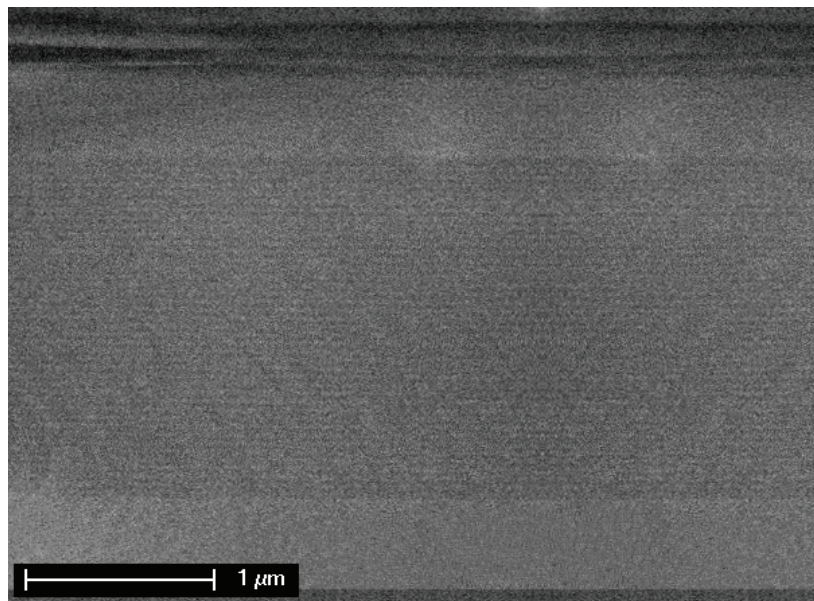


Figure 1.7: SEM of excited state QC stack and waveguide. From bottom to top, color separations are seen representing the InP substrate, $\text{In}_{0.53}\text{Ga}_{0.47}\text{As}$ bottom cladding, 40 period QC stack, $\text{In}_{0.53}\text{Ga}_{0.47}\text{As}$ top cladding, and InP top cladding.

calibration; the active core thickness showed the $\text{Al}_{0.48}\text{In}_{0.52}\text{As}$ growth rate was slow by a factor of 0.80 from the original calibration.

To confirm accuracy of our post-calibrated structure, we analyzed the wafer with high resolution double crystal X-ray diffraction. X-ray data show the primary InP reflection along with five satellite peaks that correspond to the QC core periodicity. Analysis of the satellite peak positions shows a QC period length of 489.2 Å with lattice mismatch of 0.04%. Our post-growth SEM-based characterization resulted in a period length of 511.3 Å. In comparing these two numbers, it is important to note that X-ray data was taken for a sample from the wafer edge, which generally has thinner layer thicknesses than the “prime real estate” of the wafer center. The data set as a whole is consistent, since such a narrowing in layer thickness from center to edge is standard in MBE-grown material.

Lasers were processed as deep-etched ridge waveguides with stripe widths ranging from 9 to 15 μm by conventional photolithography and wet chemical etching, and were electrically insulated by 0.3 μm thick SiN_x . After evaporation of a Ti/Au (30 nm / 300 nm) top contact, the sample was thinned to ~200 μm and a back Ge/Au (30 nm / 300 nm)

contact was deposited. Laser bars were cleaved, mounted epitaxial-side up on Cu heat sinks with In solder, and wire bonded. Electroluminescence (semi-circular cleaved-mesa) devices were also fabricated.

1.4 Device Emission Characteristics

1.4.1 Electroluminescence & Transition Identification

Emission spectra for EL mesa structures were collected using an FTIR spectrometer in step scan mode. EL data are summarized in Fig. 1.8 for heat sink temperatures T_{sink} at 80, 120, and 160 K. The data clearly show two distinct emission peaks, one near $\lambda \approx 8 \mu\text{m}$ and one near $\lambda \approx 10 \mu\text{m}$. At higher injection currents, higher photon energy emission is observed near $\lambda \approx 6.5 \mu\text{m}$. The two primary emission peaks have features largely independent of each other. As both injection current and temperature increase, the $\sim 8 \mu\text{m}$ emission gets stronger in relation to the $\sim 10 \mu\text{m}$ emission. Fitting Lorentzian line shapes to the individual peaks helps further quantify distinguishing characteristics. As electric field changes, a clear Stark tuning is present for both emission peaks; however, the peaks tune in opposite directions. As indicated in Fig. 1.8 for $T_{sink} = 80 \text{ K}$ and explicitly plotted in Fig. 1.9, the $\sim 10 \mu\text{m}$ emission blue-shifts from 118 to 134 meV over an increasing applied field range of 15 kV/cm, while the $\sim 8 \mu\text{m}$ emission red-shifts from 156 to 152 meV over the same field range. Such field-dependent behavior suggests that the $\sim 10 \mu\text{m}$ emission results from a transition that is rather diagonal in nature, while the $\sim 8 \mu\text{m}$ emission is from a transition that is more vertical. The spectral widths of each peak additionally support diagonal and vertical origins for the ~ 10 and $\sim 8 \mu\text{m}$ peaks. At $E_{field} = 72 \text{ kV/cm}$, the $\sim 10 \mu\text{m}$ emission ($\hbar\omega_{ph} = 125.6 \text{ meV}$) has a FWHM $\delta\mathcal{E}_{ul} = 18.7 \text{ meV}$ $\left(\frac{\hbar\omega_{ph}}{\delta\mathcal{E}_{ul}} = 14.9\%\right)$ and the $\sim 8 \mu\text{m}$ emission ($\hbar\omega_{ph} = 152.9 \text{ meV}$) has $\delta\mathcal{E}_{ul} = 16.2 \text{ meV}$ $\left(\frac{\hbar\omega_{ph}}{\delta\mathcal{E}_{ul}} = 10.6\%\right)$. Because diagonal transitions are more heavily influenced by interface roughness, such transitions are expected to be spectrally broader [13].

We identified the origin of the two transitions within the active region structure using the properties and behavior of the EL emission. We calculated the energies and field-dependent behavior of all possible optical transitions within the structure, and in

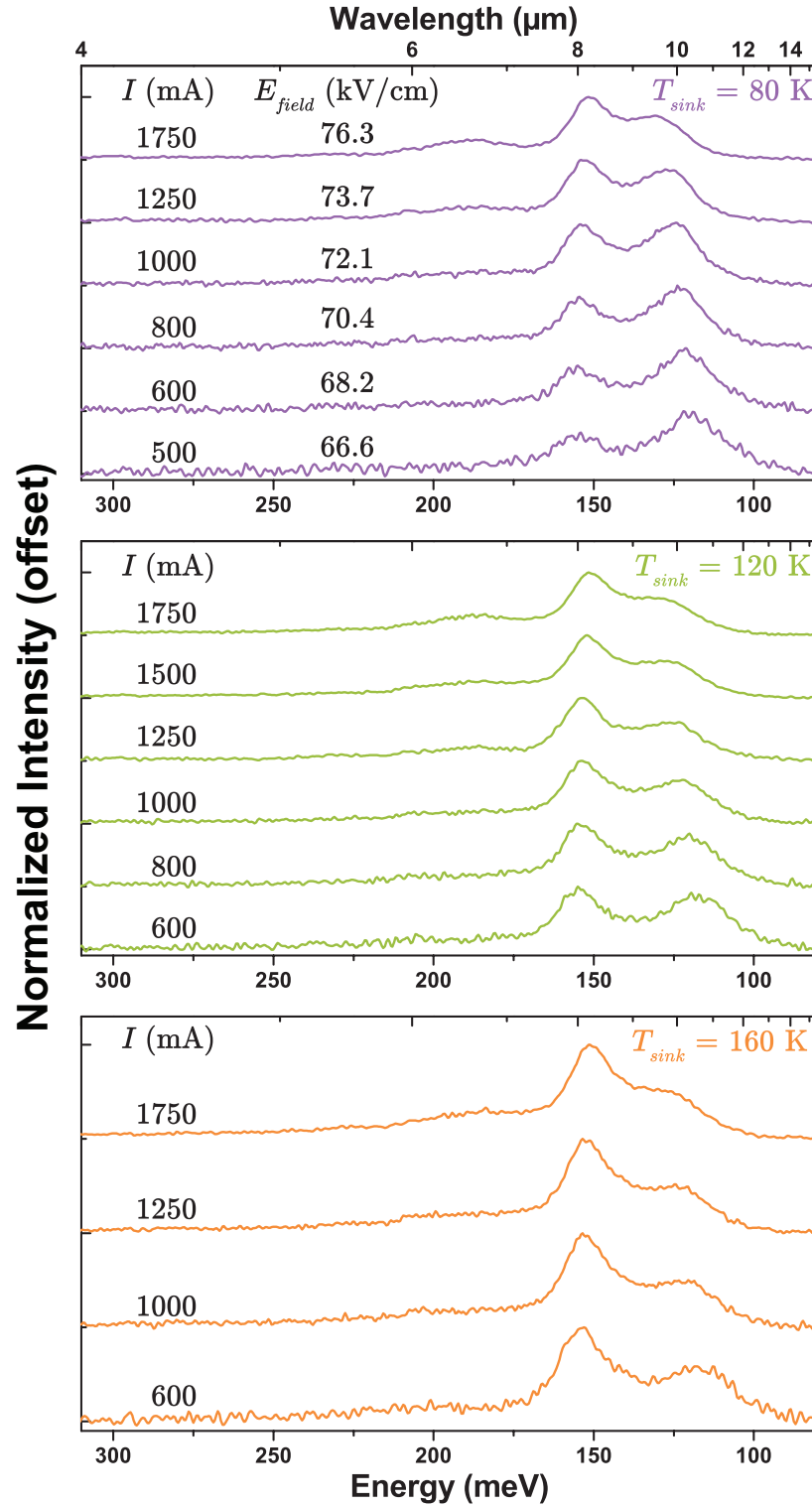


Figure 1.8: Excited state structure electroluminescence spectra. Electroluminescence spectra from a 0.027 mm² semi-circular mesa. Data were taken with current pulse width $t_{\text{pulse}} = 100$ ns at an 80 kHz repetition rate.

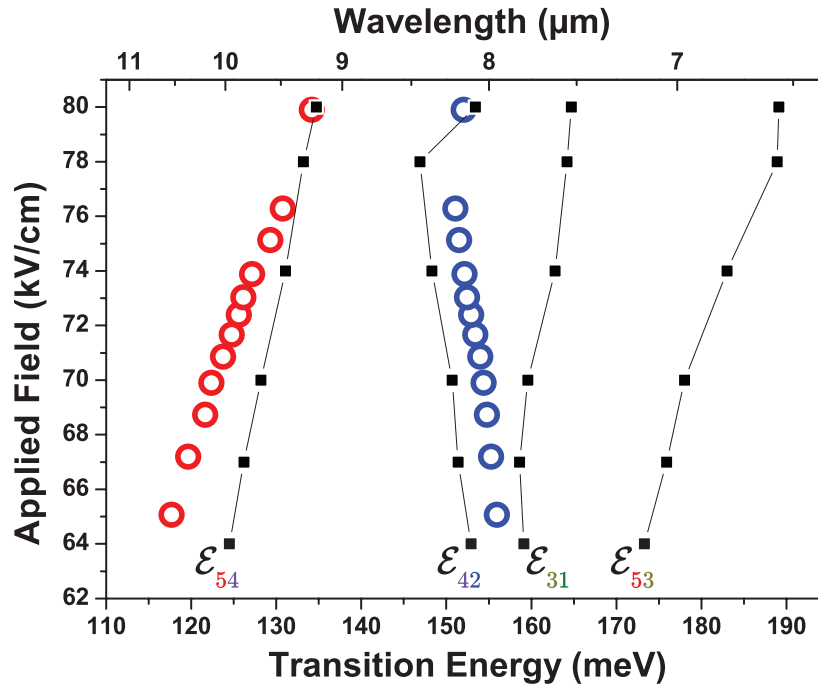


Figure 1.9: Excited state transition identification. Measured and calculated values of the optical transition energies in EL as a function of the electric field. Hollow circles represent the center points of multi-Lorentzian fits to the EL data as displayed in Fig. 1.8 for $T_{sink} = 80$ K. Solid squares show the calculated transition energies.

Fig. 1.9, we show this data for the transitions $|5\rangle \rightarrow |4\rangle$, $|4\rangle \rightarrow |2\rangle$, $|3\rangle \rightarrow |1\rangle$, and $|5\rangle \rightarrow |3\rangle$. As expected, our designed excited state $|5\rangle \rightarrow |4\rangle$ transition is the source of the $10\ \mu\text{m}$ light. Because both the field-dependent behavior and energies of the $|5\rangle \rightarrow |3\rangle$ and $|3\rangle \rightarrow |1\rangle$ transitions differ from the EL and laser spectra, we rule out these two transitions as the source of the $\sim 8\ \mu\text{m}$ light. We thus identify the source of the $\sim 8\ \mu\text{m}$ light to be the $|4\rangle \rightarrow |2\rangle$ transition; the unique field tuning behavior and the match in emission energy between observed and calculated data are in good agreement.

As further verification of the accuracy of our calculations, we examined EL at high pumping current (2.5 A, 80 kV/cm). Here, we observe five EL peaks, as shown with fitted Lorentzians in Fig. 1.10. We find excellent agreement between these peak positions and the calculated energies for the $|5\rangle \rightarrow |4\rangle$, $|5\rangle \rightarrow |3\rangle$, $|5\rangle \rightarrow |2\rangle$, $|4\rangle \rightarrow |2\rangle$, and $|4\rangle \rightarrow |1\rangle$ transitions. We note that transitions from state $|3\rangle$ are absent ($\mathcal{E}_{32} = 100.6$ meV and

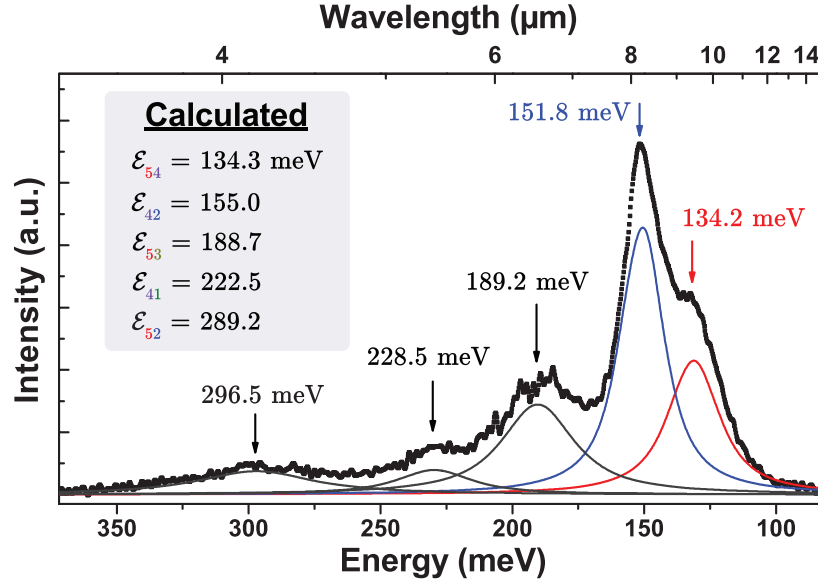


Figure 1.10: EL at high pumping current. At $T_{\text{sink}} = 80$ K and for $t_{\text{pulse}} = 100$ ns, the EL spectra at 2.5 A for a 0.027 mm^2 device is fitted with five Lorentzian peaks. The spectrum is shown without correction for detector responsivity. Calculated transition energies are given for an electric field $E_{\text{field}} = 80$ kV/cm and are in excellent agreement with the data.

$\mathcal{E}_{31} = 163.4$ meV). This is most likely due to a lack of electrons available to populate state $|3\rangle$ as an optical transition upper state.

1.4.2 Laser Emission

We observe lasing from both transitions associated with the primary EL peaks $|5\rangle \rightarrow |4\rangle$ and $|4\rangle \rightarrow |2\rangle$. Like with EL emission behavior, the two laser lines have distinctive and separate behavior. Fig. 1.11 shows laser emission at $T_{\text{sink}} = 80$ K for a range of injection currents and pulse widths. Noting that FTIR spectra are time-integrated, the emission changes from strongly favoring the $|5\rangle \rightarrow |4\rangle$ transition to strongly favoring the $|4\rangle \rightarrow |2\rangle$ transition by changing the current pulse width t_{pulse} from 10 to 100 ns. That is, for $t_{\text{pulse}} = 10$ ns, the $|4\rangle \rightarrow |2\rangle$ transition does not lase for $I \leq 1.7$ A; for $t_{\text{pulse}} = 100$ ns, the $|4\rangle \rightarrow |2\rangle$ threshold appears to be less than that of $|5\rangle \rightarrow |4\rangle$. Simultaneous lasing of both the $|5\rangle \rightarrow |4\rangle$ and $|4\rangle \rightarrow |2\rangle$ transition is seen for much of the parameter space.

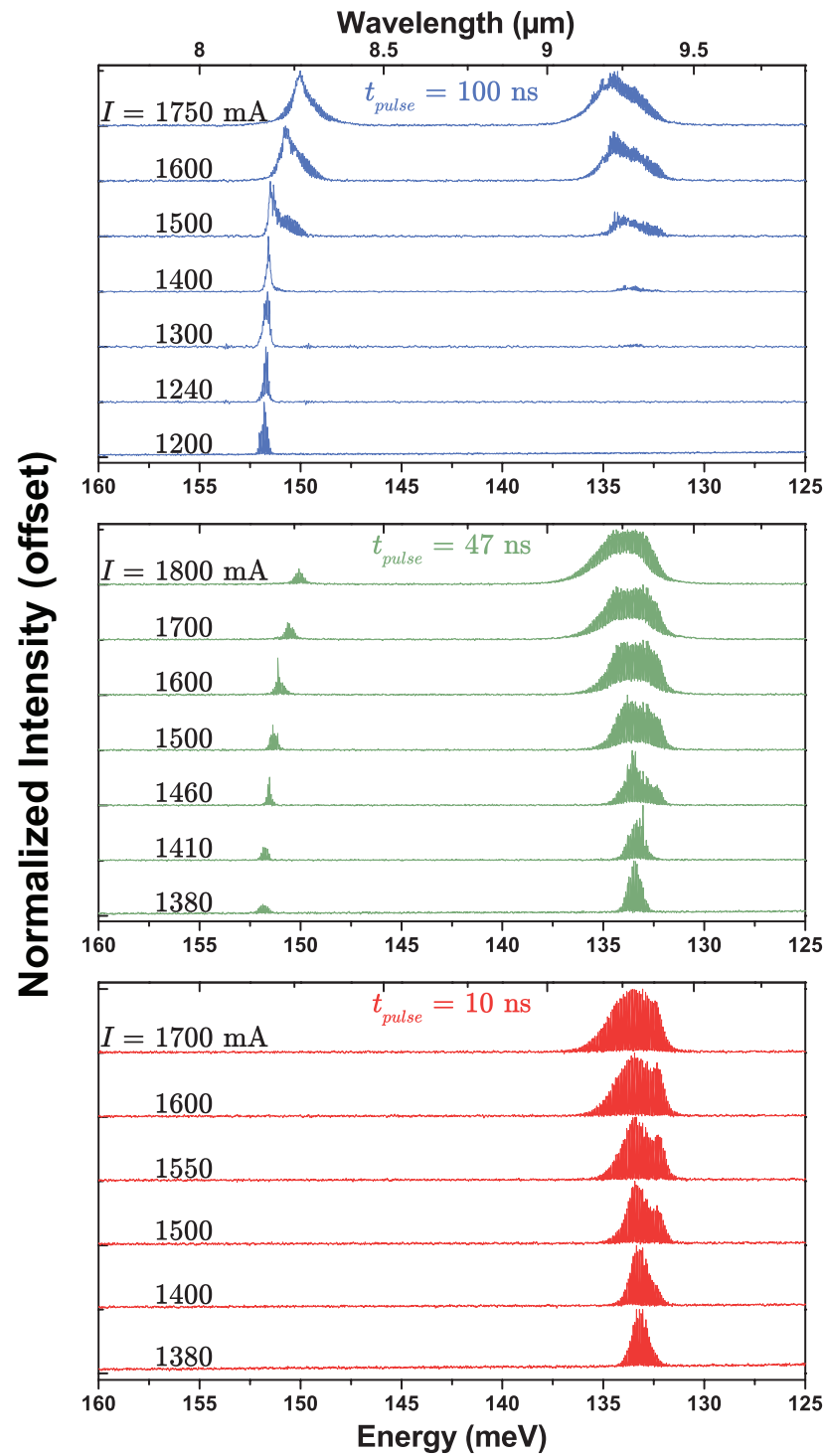


Figure 1.11: Excited state laser spectra. Pulsed lasing spectra for a 2.5 mm \times 10 μ m laser ridge at a heat sink temperature $T_{sink} = 80$ K. Current pulse widths t_{pulse} were 10, 47, and 100 ns at an 80 kHz repetition rate.

1.4.3 Stacked Transitions (?)

Knowing our laser transitions are $|5\rangle \rightarrow |4\rangle$ and $|4\rangle \rightarrow |2\rangle$, a re-examination of the band structure in Fig. 1.6 illustrates how these transitions are energetically “stacked.” Indeed, with simultaneous lasing of both transitions, this appears to be the “cascaded” transition setup sought by C. Sirtori *et al.* [13] for producing correlated photons. Besides the production of correlated photons, such stacked transitions could be useful for ultra-low noise spectroscopy applications, where the system noise of a secondary laser line is used to subtract out noise sources present in the laser line of primary interest. Such an ability would result from the carrier populations of the two transitions being inherently linked.

While these applications certainly make the energy configuration represented in the Fig. 1.6 band diagram highly interesting, the spectral data presented so far point to a glaring problem with the interpretation. In a relative sense, both EL and laser spectra show that when one transition gets stronger, the other gets weaker. In the simple stacked transition picture, one would intuitively think that if one transition gets stronger, the other transition would also get simultaneously stronger; more carriers for one transition should yield carriers for the other. In contrast to such output power behavior that is correlated, we observe just the opposite: anti-correlated behavior in output power.

1.5 Anti-correlated Light Output Behavior

Knowing that the two laser lines in the structure are substantially separated in wavelength, short-pass ($\lambda_{pass} < 8.70 \mu\text{m}$) and long-pass ($\lambda_{pass} > 8.65 \mu\text{m}$) filters were used to more thoroughly examine light vs. current (LI) characteristics of the laser devices. In the LI data, the distinctive behavior of each transition becomes even more apparent, with light output and thresholds showing evident differences with remarkable temperature dependencies.

Light from the $|5\rangle \rightarrow |4\rangle$ transition shows a behavior typical of a QC laser intersubband optical transition and is rather unremarkable. As indicated in Figs. 1.12a and 1.13, the highest output power and lowest threshold currents are achieved at the lowest temperatures. With increasing temperature, shorter non-radiative transition times, thermal population of the lower laser state, thermionic emission from the upper laser state, and decreased upper laser level injection efficiency make obtaining population

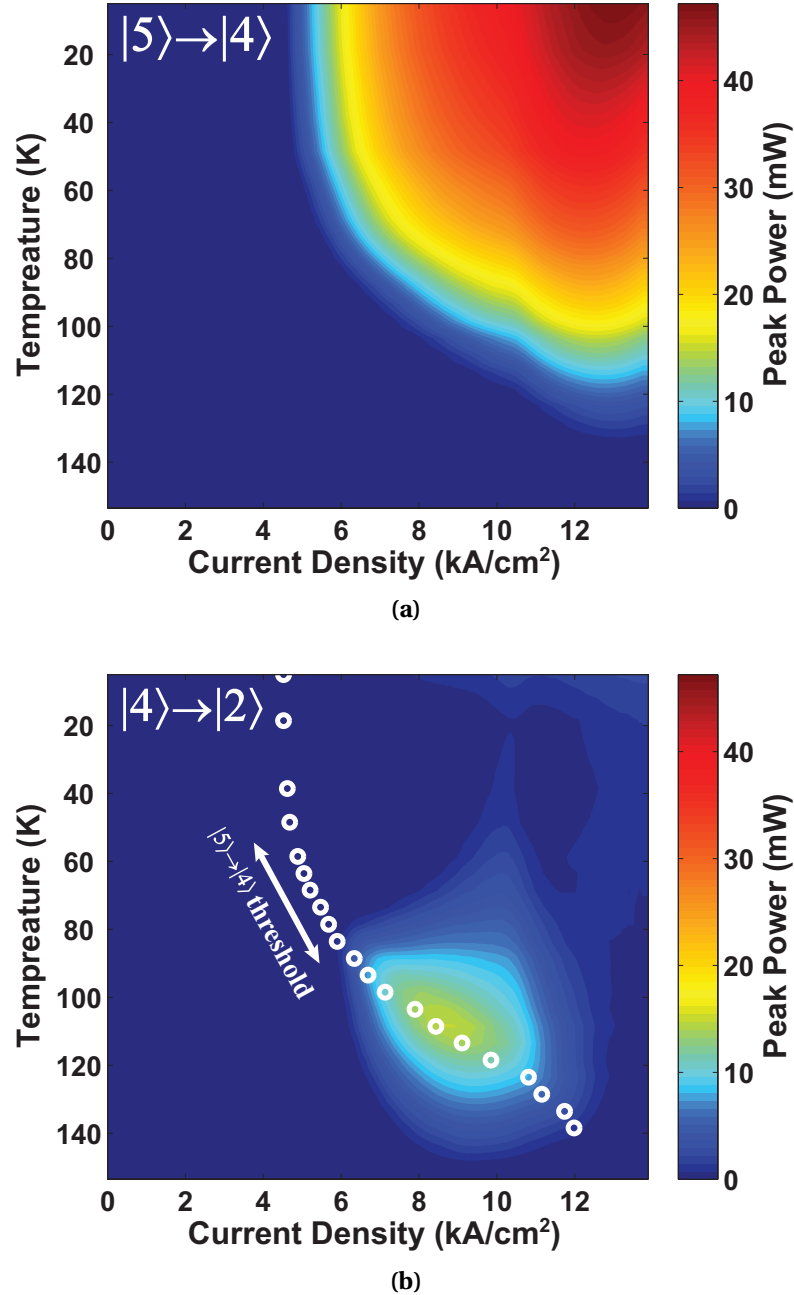


Figure 1.12: Light output characteristics of a representative laser device. Light output versus current density and heat sink temperature of a $1.48 \text{ mm} \times 12.1 \text{ }\mu\text{m}$ laser for the (a) $|5\rangle \rightarrow |4\rangle$ and (b) $|4\rangle \rightarrow |2\rangle$ transitions. Data shown for the $|5\rangle \rightarrow |4\rangle$ transition are consistent with standard QC laser behavior. In contrast, the $|4\rangle \rightarrow |2\rangle$ transition operates poorly at the lowest heat sink temperatures; the transition instead has a thermally induced peak performance near 115 K. With the $|5\rangle \rightarrow |4\rangle$ transition threshold (white circles) overlaid on (b), it can be seen that the $|4\rangle \rightarrow |2\rangle$ roll-off is coincident with $|5\rangle \rightarrow |4\rangle$ turn-on.

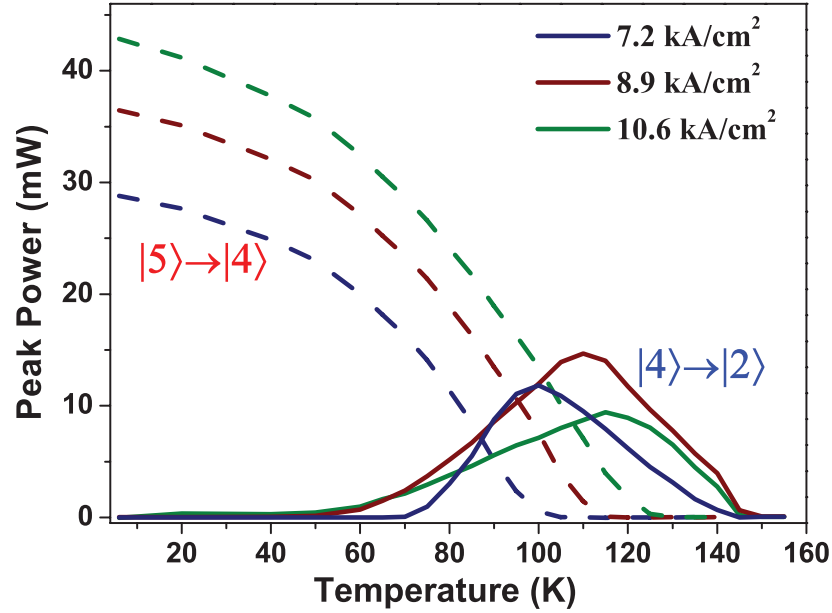


Figure 1.13: Light-temperature cross-sections. Spectrally resolved light output for three fixed pumping current densities with increasing temperature. The $|5\rangle \rightarrow |4\rangle$ transition is shown with dashed lines and the $|4\rangle \rightarrow |2\rangle$ transition is shown with solid lines. The $|4\rangle \rightarrow |2\rangle$ transition output is affected the the $|5\rangle \rightarrow |4\rangle$ transition output power.

inversion more difficult. Consequently stronger pumping is required to achieve laser action, until a temperature is reached where the laser is unable to achieve threshold, in this case near $T_{sink} = 125$ K [14]

The lower $|4\rangle \rightarrow |2\rangle$ transition deviates from the familiar intersubband optical transition behavior significantly. Most strikingly, the transition lases more effectively at elevated temperatures (near $T_{sink} = 100$ K), while performance is substantially diminished at lower temperatures. As shown in Figs. 1.12b and 1.13 for a $1.48 \text{ mm} \times 12.1 \text{ }\mu\text{m}$ device, lasing onset is induced near 60 K. Peak output power with constant current density *increases* with temperature up to 115 K, while threshold current simultaneously *decreases*. For temperatures above 115 K, a more typical thermal roll-over in power is observed. The light-current curves in Fig. 1.14 reveal more: a threshold “crossover” is observed at 85 K, above which point the $|4\rangle \rightarrow |2\rangle$ transition develops a lower threshold than the $|5\rangle \rightarrow |4\rangle$ transition. At temperatures below this crossover, if the $|4\rangle \rightarrow |2\rangle$ transition is lasing, the $|5\rangle \rightarrow |4\rangle$ transition is also lasing. After the crossover and for low pumping rates, a regime exists where only the lower $|4\rangle \rightarrow |2\rangle$ transition lases. However, as

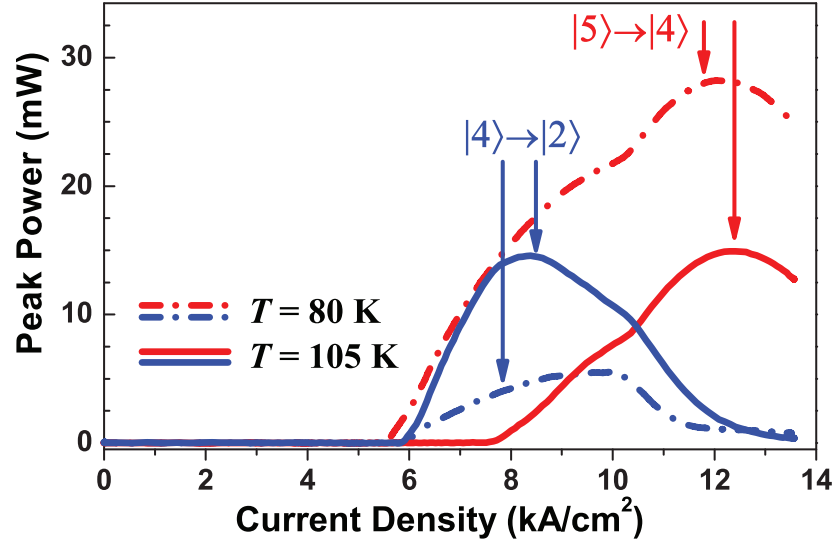


Figure 1.14: Light-current cross-sections. For each optical transition, light-current curves are shown at 80 and 105 K. A crossover in laser thresholds occurs at 85 K, where the $|4\rangle \rightarrow |2\rangle$ transition achieves a lower threshold than the $|5\rangle \rightarrow |4\rangle$ transition. At 105 K, transition $|4\rangle \rightarrow |2\rangle$ has the lower threshold; here, the $|5\rangle \rightarrow |4\rangle$ transition threshold marks the beginning of the $|4\rangle \rightarrow |2\rangle$ power roll-off.

soon as the upper $|5\rangle \rightarrow |4\rangle$ transition reaches threshold, an abrupt drop in $|4\rangle \rightarrow |2\rangle$ output power is observed. This anti-correlation in output power between the two transitions persists even above threshold. The Fig. 1.15 plot of thresholds shows that after crossover, the $|4\rangle \rightarrow |2\rangle$ transition threshold takes on a more typical QC laser behavior, having a characteristic temperature $T_0 \approx 220$ K; before crossover, however, the transition has a *negative* characteristic temperature $T_0 \approx -66$ K! The sharp “kink” in the $|4\rangle \rightarrow |2\rangle$ transition threshold at the crossover point along with the anti-correlated output power behavior are indicative of a strong interaction between the carrier populations of the two optical transitions.

For a thorough study of the structure, along with preliminary characterization of multiple (~ 30) laser devices, we performed full, detailed, temperature-dependent characterizations on six different lasers from different parts of the wafer. Cavity lengths were 1.38, 1.48, 1.50, 1.63, 1.93, and 2.28 mm. All data sets showed device characteristics similar to the data presented in Figs. 1.12–1.15. All devices showed anti-correlated behavior between two competing optical transitions lasing near $\lambda \approx 9.5$ μm and 8.2 μm . Also, a stronger $|5\rangle \rightarrow |4\rangle$ transition always led to a weaker $|4\rangle \rightarrow |2\rangle$ transition.

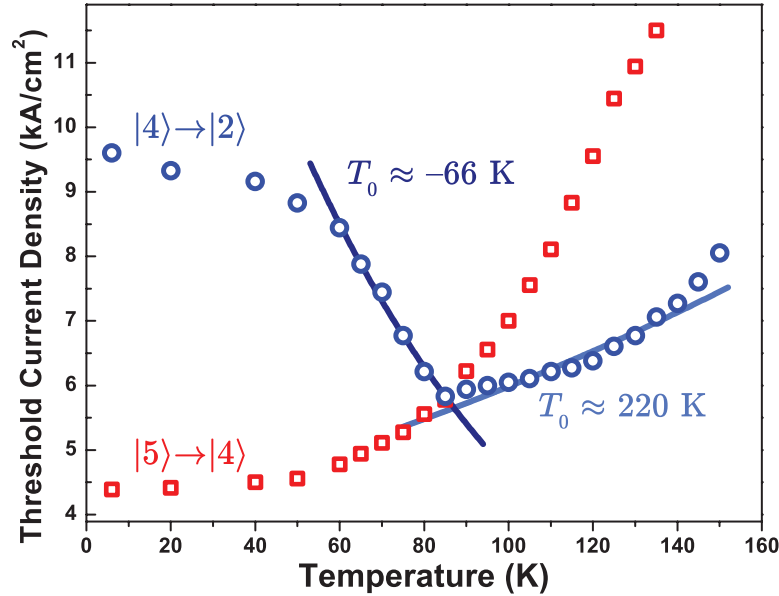


Figure 1.15: Threshold temperature-dependence of the transitions. Red symbols indicate observed threshold current densities for the $|5\rangle \rightarrow |4\rangle$ transition and blue symbols the $|4\rangle \rightarrow |2\rangle$ transition. A crossover in thresholds is seen near 85 K. Before this crossover, the $|4\rangle \rightarrow |2\rangle$ transition threshold decreases with increasing temperature, giving a negative characteristic temperature ($T_0 \approx -66$ K). After the crossover, the $|4\rangle \rightarrow |2\rangle$ transition has a more conventional $T_0 \approx 220$ K.

1.6 Lasing High in k -Space

The simple stacked transition representation suggested by Fig. 1.6 cannot account for the observed anti-correlated behavior in output power. As earlier mentioned, such a stacked transition scheme would more directly lead to correlated—rather than anti-correlated—behavior in output power. Our typical representation of the energy band configuration, such as in Fig. 1.6, hides many characteristics of the system. Specifically, the system only has energy state quantization in one dimension, the direction of epitaxial growth. In the other two (“in-plane”) dimensions, electrons are free to take on a much broader range of momentum (and therefore energy) values. The in-plane freedom creates an energy dispersion of the individual subbands of roughly parabolic form. Generally, any consideration of such dispersion is neglected in our energy band diagrams, since only the energy values at the energy band minima—the Γ point ($k = 0$)—are indicated by the plot. In most cases, the simple picture is good enough, since most

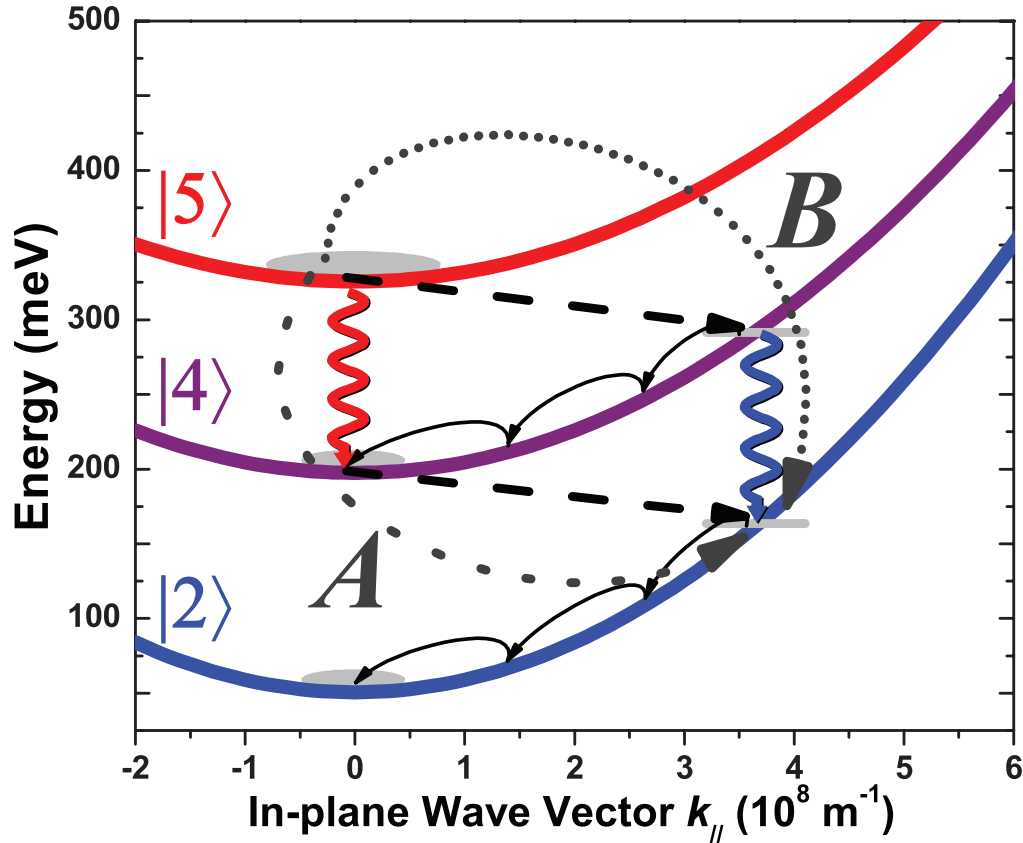


Figure 1.16: The k -space electron paths. The in-plane k -space dispersion $k_{||}$ of the subbands $|5\rangle$, $|4\rangle$, and $|2\rangle$ is shown. Electrons being injected into state $|5\rangle$ can follow either path A (the $|5\rangle \rightarrow |4\rangle$ optical transition) or path B (the $|4\rangle \rightarrow |2\rangle$ optical transition preceded by LO phonon scattering). Path A is typical for a QC laser transition, and path B represents the high k -space transition. Optical transitions are indicated by wavy arrows, intersubband phonon transitions are shown with dashed-line arrows, intrasubband scattering is shown with curved arrows, and paths A and B are shown with dotted arrows. Local k -space minima (i.e., “electron pools”) are shown as gray areas.

opto-electronic devices operate using electrons in a quasi-equilibrium state, or in a state where electrons are able to “pool” for a long time relative to other relevant system times.

The data presented in the previous sections require that we envision a mode of operation whereby a second optical transition is in competition with a first transition for charge carriers. In a QC structure such as ours, we arrive at the model schematically depicted in Fig. 1.16: the secondary laser transition is a vertical transition between subbands, positioned high in k -space. Given the three identified energy subbands

$|5\rangle$, $|4\rangle$, and $|2\rangle$, several different electron transport paths are possible; two are labeled A and B . Path A is characteristic for a QC laser optical transition, where electrons undergo a radiative transition followed by LO phonon scattering. When the $|5\rangle \rightarrow |4\rangle$ transition is lasing, large cavity photon densities at the $|5\rangle \rightarrow |4\rangle$ transition energy and strong stimulated emission ensure that this is the dominant electron path. However, at elevated temperatures, path B becomes available with increased LO phonon scattering out of state $|5\rangle$, populating state $|4\rangle$ high in k -space. In the situation where path A is “off” because threshold has not yet been reached for the $|5\rangle \rightarrow |4\rangle$ transition, carriers are provided so that lasing can occur at high k -space for the $|4\rangle \rightarrow |2\rangle$ transition. If at any time path A turns on, path B and therefore $|4\rangle \rightarrow |2\rangle$ population inversion is suppressed because

- (i) fewer electrons are available to populate the upper state of the high k -space $|4\rangle \rightarrow |2\rangle$ optical transition and
- (ii) electrons are injected into the lower state of the high k -space $|4\rangle \rightarrow |2\rangle$ transition.

Moreover, if transport through path A is slowed due to a weakening $|5\rangle \rightarrow |4\rangle$ laser transition, path B will concurrently see an enhancement of available electrons able to contribute to $|4\rangle \rightarrow |2\rangle$ lasing. This effect accounts for the dramatic decrease in $|4\rangle \rightarrow |2\rangle$ threshold from 55 to 85 K. The observed anti-correlated behavior of the two transitions is thus sustained. It is worth noting that this anti-correlated transport picture implies that the $|4\rangle \rightarrow |2\rangle$ transition has only “local” population inversion; that is, population inversion does not exist globally over the entire subbands $|4\rangle$ and $|2\rangle$. This is not the first time local population inversion has been reported. J. Faist *et al.* reported such local inversion in 1996 [15]. However, their report detailed local inversion at $k = 0$. In contrast, our structure does not attain inversion at $k = 0$ at all, and instead only reaches a local population inversion at high k -space values.

The energy subband dispersion $\mathcal{E}_n(k_{||})$ plotted in Fig. 1.16 for subbands n incorporates the energy dependence of the effective mass. We define $\mathcal{E}_n(k_{||})$ relative to the conduction band edge as $\mathcal{E}_n(0)$ (the subband energy at $k = 0$) plus a dispersion term $\delta\mathcal{E}_n(k_{||})$,

$$\mathcal{E}_n(k_{||}) = \mathcal{E}_n(0) + \delta\mathcal{E}_n(k_{||}) \quad (1.6)$$

and

$$\delta\mathcal{E}_n(k_{//}) = \frac{\hbar^2 k_{//}^2}{2m^*(\mathcal{E}_n(k_{//}))} = \frac{\hbar^2 k_{//}^2}{2\left(1 + \frac{\mathcal{E}_n(0) + \delta\mathcal{E}_n(k_{//})}{\mathcal{E}_G^\Gamma}\right)m_e^*} \quad (1.7)$$

using here the empirical approach of Nelson *et al.* [16] where $m^*(\mathcal{E}) = \left(1 + \frac{\mathcal{E}}{\mathcal{E}_G^\Gamma}\right)m_e^*$. In the calculation for Fig. 1.16, we use a Γ -point bandgap $\mathcal{E}_G^\Gamma = 0.784$ eV (which corresponds to a non-parabolicity parameter $\gamma = \frac{\hbar^2}{2m_e^*\mathcal{E}_G^\Gamma} = 1.13 \times 10^{-14} \text{ cm}^2$ [17]) and assume the band-edge effective mass to be that of the $\text{In}_{0.53}\text{Ga}_{0.47}\text{As}$ well ($m_e^* = 0.043m_e$).

Making the assumption that $\hbar\omega_{LO} = 34$ meV, electrons scattering out of state $|5\rangle$ (at $k = 0$) into state $|4\rangle$ via LO phonons acquire a k -space value $k_{//} = 3.6 \times 10^8 \text{ m}^{-1}$. We therefore infer that the observed high k -space lasing occurs near $k_{//} = 3.6 \times 10^8 \text{ m}^{-1}$, which is further supported by evidence described in the next section. It is worthwhile to note that at $k_{//} = 3.6 \times 10^8 \text{ m}^{-1}$, $\delta\mathcal{E}_4(k_{//}) \approx 90$ meV, giving about three LO phonon intrasubband scattering events before the electron reaches the quasi-equilibrium point at $k = 0$. Likewise, $\delta\mathcal{E}_2(3.6 \times 10^8 \text{ m}^{-1}) \approx 113$ meV, again giving roughly three LO phonon events before the a high k -space electron reaches the quasi-equilibrium point in subband $|2\rangle$.

This energy-dependence of the effective mass results in “non-parabolicity” of the energy subbands, a diversion of the energy subband from the truly parabolic shape proportional to $k_{//}^2$ when effective mass has no energy dependence. In our particular device, this non-parabolicity effect results in some highly interesting consequences.

1.7 Effects of Non-parabolicity

Of particular interest for such a high k -space transition is the affect of energy subband non-parabolicity [18]. At the Brillouin zone center $k = 0$, energy subbands have a substantially parabolic form. However, non-parabolicity implies that, with both increasing k and increasing subband energy above the band edge, the subbands flatten [17]. This non-parabolicity has spectral consequences: for a transition between two subbands, the transition energy decreases as the transition occurs at higher k values. For the $|4\rangle \rightarrow |2\rangle$ transition in our structure, we calculate that photons generated at $k_{//} = 3.6 \times 10^8 \text{ m}^{-1}$ will have 16.1 meV less energy than photons generated at $k = 0$.

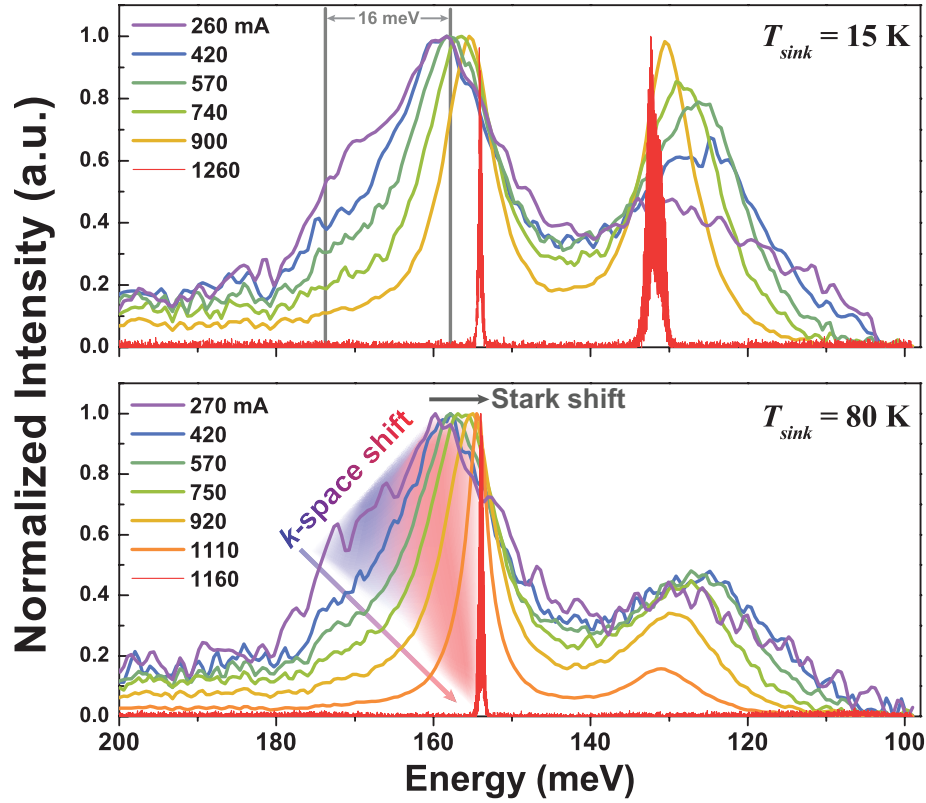


Figure 1.17: Spectral signature of k -space emission. Spectral behavior of a $1.93 \text{ mm} \times 9.4 \text{ }\mu\text{m}$ laser at 15 and 80 K, with the $|4\rangle \rightarrow |2\rangle$ transition emission centered around 160 meV. Resulting from subband non-parabolicity, high k -space emission has less photon energy than emission from $k = 0$. For the $|4\rangle \rightarrow |2\rangle$ transition, the broad emission with pronounced asymmetry at low injection currents is indicative of optical emission originating from a distribution of k values. As the injection current increases, the transition preferentially emits photons at the low-energy edge of the distribution—that is, from high in k -space.

Sub-threshold spectral data, as shown in Fig. 1.17 for a $1.93 \text{ mm} \times 9.4 \text{ }\mu\text{m}$ laser, reveal such a k -space spectral signature. For the $|4\rangle \rightarrow |2\rangle$ emission around 160 meV, we observe two effects that contribute to a spectral red-shift. Over a range of injection currents that spans deeply sub-threshold to just above threshold, Stark tuning shifts the peak emission by $\sim 5.5 \text{ meV}$. More interestingly, at low injection currents, the $|4\rangle \rightarrow |2\rangle$ emission exhibits pronounced asymmetry. At the lowest injection currents, the spectral width is quite broad: about 16 meV. As injection current is increased, the higher energy side of the emission collapses; the transition strongly favors emission on the side of low energy. Also, as injection current is increased, the emission asymmetry gives way to a

more typical Lorentzian-shaped emission. Thus, for a laser device where cavity effects strongly influence emission behavior, these spectral features are consistent with laser emission originating high in k -space.

Non-parabolic energy subbands lead to two interesting and favorable consequences for an electrically-pumped high k -space laser transition. Firstly, threshold currents are reduced due to a decrease in the primary source of optical absorption loss—that is, intersubband absorption at the lasing energy from the electron pool at $k = 0$. With a high k -space transition between non-parabolic energy subbands, the optical emission process is decoupled from the normally concurrent reverse process of optical absorption. Secondly, the presence of non-parabolicity helps achieve a more favorable lifetime profile for the $|4\rangle \rightarrow |2\rangle$ transition. Because of non-parabolicity, the energy conversion of an LO phonon requires the exchange of a larger k values for higher energy subbands, which in turn reduces the scattering rate [19] [20] [21] as $1/k^2$ [22] [23]. The influences of these effects are reflected in the results of our rate equation model. As detailed in the next section, to reconcile calculated temperature-dependent thresholds with observed data, the optical absorption loss associated with the $|4\rangle \rightarrow |2\rangle$ laser energy was decreased by about a factor of 10.

Prior work on the theory of QC laser gain spectra [24] hinted at the feasibility of such an electrically-pumped high k -space laser transition. Here, Gorfinkel *et al.* predicted the existence of local high k -space population inversion resulting purely from the presence of energy subband non-parabolicity. Because higher-energy subbands are “flatter,” the assumption of thermally-distributed k -space energy dispersion implies that an inverted population profile can exist at high k -space values even if the higher energy subband contains less total carriers than the lower subband. In the work presented in this chapter, rather than relying on a thermal distribution of electrons around $k = 0$ to populate a high k -space energy band, our excited state QC design directly injects non-quasi-equilibrium high k -space electrons.

1.8 Rate Equation Modeling

1.8.1 A Dual-Optical Transition Coupled System

To further confirm the plausibility of our k -space interpretation, we modeled our laser with a common rate equation methodology. Our rate equation model includes electron populations for six energy “levels”: four for each of the active region energy levels $|5\rangle$, $|4\rangle$, $|3\rangle$, and $|2\rangle$ in Fig. 1.6, and two high k -space regions for subbands $|4\rangle$ and $|2\rangle$. The model also includes stimulated emission terms and photon fluxes for the transitions $|5\rangle \rightarrow |4\rangle$ and $|4\rangle \rightarrow |2\rangle$. The temperature dependence of energy state lifetimes [25], injection efficiency, thermal backfilling of energy states [25], and thermionic emission [26] were all included. Using the symbolic math toolbox in Matlab, we solved the system of rate equations under steady state conditions $\left(\frac{d(\cdot)}{dt} = 0\right)$.

$$\begin{aligned}
 \frac{dn_5}{dt} &= \eta_{inj} \frac{J}{q} - n_5 \left(\frac{1}{\tau_{54}} + \frac{1}{\tau_{53}} + \frac{1}{\tau_{52}} + \frac{1}{\tau_{51}} \right) - \frac{n_5}{\tau_{therm}} - S_{54} g_{54} (n_5 - n_4) \\
 \frac{dn_{4k}}{dt} &= (1 - \eta_{inj}) \frac{J}{q} + \frac{n_5}{\tau_5} - \frac{n_4}{\tau_{k4}} - S_{42} g_{42} (n_{4k} - n_{2k}) \\
 \frac{dn_4}{dt} &= \frac{n_{4k}}{\tau_{4k}} - n_4 \left(\frac{1}{\tau_{43}} + \frac{1}{\tau_{42}} + \frac{1}{\tau_{41}} \right) + S_{54} g_{54} (n_5 - n_4) \\
 \frac{dn_3}{dt} &= \frac{n_5}{\tau_{53}} + \frac{n_4}{\tau_{43}} - n_3 \left(\frac{1}{\tau_{32}} + \frac{1}{\tau_{31}} \right) \\
 \frac{dn_{2k}}{dt} &= \frac{n_5}{\tau_{52}} + \frac{n_4}{\tau_{42}} + \frac{n_3}{\tau_{32}} - \frac{n_{2k}}{\tau_{2k}} + S_{42} g_{42} (n_{4k} - n_{2k}) \\
 \frac{dn_2}{dt} &= \frac{n_{2k}}{\tau_{2k}} - \frac{n_2}{\tau_{21}} + \frac{n_{inj} e^{-\frac{\Delta_{inj} + \varepsilon_{21}}{kT}}}{\tau_{21}} \\
 \frac{dS_{54}}{dt} &= \left(N_p g_{54} (n_5 - n_4) - \frac{1}{\tau_{ph1}} \right) S_{54} \\
 \frac{dS_{42}}{dt} &= \left(N_p g_{42} (n_{4k} - n_{2k}) - \frac{1}{\tau_{ph2}} \right) S_{42}
 \end{aligned} \tag{1.8}$$

The temperature-dependence of all energy state lifetimes $\tau_{u\ell}$ was included with the standard relation derived from by the Bose–Einstein occupation of LO phonons.

$$\frac{1}{\tau_{u\ell}(T)} = \frac{1}{\tau_{u\ell}(0)} \left(1 + \frac{2}{e^{\frac{\hbar\omega_{LO}}{k_B T}} - 1} \right) \tag{1.9}$$

Table 1.1: Parameters used in the k -space laser rate equation model.

R	0.27	L_p	511 Å
width	12 μm	N_p	40
L	1.5 mm	Δ_{inj}	27.3 meV
$\hbar\omega_{LO}$	34 meV	n_{inj}	$1.6 \times 10^{11} \text{ cm}^{-3}$
\mathcal{E}_{21}	67.4 meV	\mathcal{E}_{3c}	60 meV
w	197 Å	m^*	$0.043m_e$
Γ_{54}	0.60	Γ_{42}	0.67
α_{w54}	7.4 cm^{-1}	α_{w42}	5.2 cm^{-1}
\mathcal{E}_{54}	128 meV	\mathcal{E}_{42}	151 meV
z_{54}	23 Å	z_{42}	13 Å
$\delta\mathcal{E}_{54}$	24 meV	$\delta\mathcal{E}_{42}$	15 meV

The injection efficiency η_{inj} into the upper laser state $|5\rangle$ (and into the k -space state $|4\rangle$) [27] was treated in a similar manner.

$$\eta_{inj}(T) = \eta_{inj} \left(1 + \frac{2}{e^{\frac{\hbar\omega_{LO}}{k_B T}} - 1} \right) \quad (1.10)$$

Thermionic emission out of the upper laser state $|5\rangle$ was included using the method of S. Sze [26].

$$\tau_{therm}(T) = w \sqrt{\frac{2\pi m^*}{k_B T}} e^{\frac{\mathcal{E}_{3c}}{k_B T}} \quad (1.11)$$

The gain coefficient $g_{u\ell}$ for the transition $|u\rangle \rightarrow |\ell\rangle$ is given by

$$g_{u\ell} = \frac{c\Gamma_{u\ell}}{N_p n_{eff}} \frac{2q^2 \mathcal{E}_{u\ell} z_{u\ell}^2}{h c \epsilon_0 n_{eff} \delta\mathcal{E}_{u\ell} L_p} \quad (1.12)$$

and the photon lifetime with the cavity for the transition $|u\rangle \rightarrow |\ell\rangle$ is

$$\tau_{ph,u\ell} = \frac{n_{eff}}{c \left(-\frac{1}{L} \ln(R) + \alpha_{w,u\ell} \right)}. \quad (1.13)$$

The parameters used for the calculation are given in Tables 1.1 and 1.2.

Table 1.2: Calculated LO phonon lifetimes at $T = 0$ K used in the k -space laser rate equation model.

$\tau_{u\ell}$ (ps)	upper state u			
	5	4	3	2
lower state ℓ	4	4.0		
	3	4.2	1.2	
	2	7.0	1.9	3.0
	1	9.3	10.6	3.5

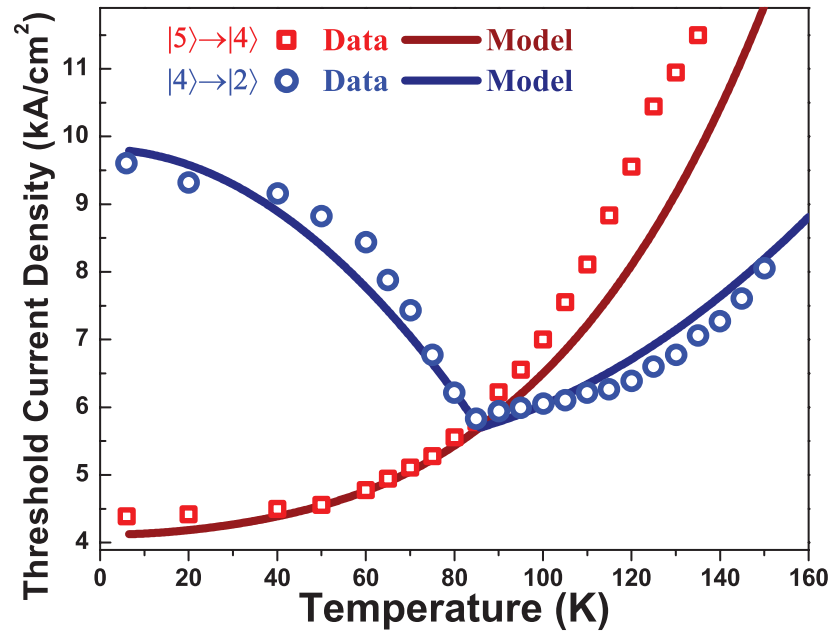


Figure 1.18: Model results for transition thresholds. Observed and modeled temperature-dependent threshold current densities for the two optical transitions. Red symbols indicate thresholds for the $|5\rangle \rightarrow |4\rangle$ transition and blue symbols the $|4\rangle \rightarrow |2\rangle$ transition. A crossover in thresholds is seen near 85 K. Before this crossover, the $|4\rangle \rightarrow |2\rangle$ transition threshold decreases with increasing temperature. A sharp kink is observed in the $|4\rangle \rightarrow |2\rangle$ threshold when it becomes lower than that of the transition $|5\rangle \rightarrow |4\rangle$. These features are reproducible with a conventional QC rate equation model with temperature-dependent parameters, the results of which are indicated by solid lines.

Table 1.3: Fitting parameters used to match the k -space rate equation model to observed data.

	scaling value	final value
α_{w54}	4.6	34 cm^{-1}
α_{w42}	0.1	0.52 cm^{-1}
η_{inj}		0.88

1.8.2 Comparing Threshold Data with Simulation

Threshold current densities provide direct means for comparing observed data with the model results. In using our rate equation model to find threshold current densities, we look for roots of the expression $S_{u\ell}(J)$ as a function of temperature; that is, when $S_{u\ell}(J) = 0$, we have a threshold condition. Figure 1.18 shows a comparison of observed data (open symbols) and calculated thresholds (solid lines). Using three fitting parameters, our rate equation model is able to provide an excellent reproduction of our observed data. The three fitting parameters used each control primarily one “feature” of the plotted data. First, by scaling the $|5\rangle \rightarrow |4\rangle$ waveguide loss α_{w54} , we match the observed and calculated values of threshold current density for transition $|5\rangle \rightarrow |4\rangle$ over the full temperature range. Second, by scaling the $|4\rangle \rightarrow |2\rangle$ waveguide loss α_{w42} , we match the observed and calculated values of threshold for $|4\rangle \rightarrow |2\rangle$ for $T > 85 \text{ K}$. This is the temperature range where transition $|4\rangle \rightarrow |2\rangle$ behaves like a conventional QC transition, and where transport through the transition $|5\rangle \rightarrow |4\rangle$ lasing channel is not available since $|5\rangle \rightarrow |4\rangle$ has yet to reach threshold. Our final fitting parameter is the injection efficiency η_{inj} into state $|5\rangle$ and the k -space state $|4\rangle$. Decreasing η_{inj} has the effect of increasing the separation in thresholds for the two transitions for $T < 85 \text{ K}$.

To achieve the fit between observed and calculated data shown in Fig. 1.18, α_{w54} was scaled by a factor of 4.6, α_{w42} was scaled by a factor of 0.1, and η_{inj} was set to 0.88. The large scaling factor for the transition $|5\rangle \rightarrow |4\rangle$ loss is not surprising, since free carrier loss calculated by the Drude model usually results in an under-estimate [28]. The extremely small scaling factor for the transition $|4\rangle \rightarrow |2\rangle$ loss needed to reconcile observed and calculated thresholds reflects the effects of k -space non-parabolicity described in Section 1.7.

We were particularly keen on confirming that a k -space transition model could reproduce three key features observed in the threshold behavior of the $|5\rangle \rightarrow |4\rangle$ and $|4\rangle \rightarrow |2\rangle$ transitions; those were (i) the unconventional threshold behavior of the $|4\rangle \rightarrow |2\rangle$ laser transition that decreases then increases with temperature; (ii) the crossing of the $|5\rangle \rightarrow |4\rangle$ and $|4\rangle \rightarrow |2\rangle$ laser thresholds; and (iii) the sharp kink in the temperature-dependent evolution of the $|4\rangle \rightarrow |2\rangle$ transition threshold at the crossover point. As clearly seen in Fig. 1.18, the k -space rate equation model is able to accurately reproduce these key features.

A more thorough understanding of the model details may be useful in understanding the origin of the rapid decrease in transition $|4\rangle \rightarrow |2\rangle$ threshold in the 50–85 K temperature range and the sharp kink in the $|4\rangle \rightarrow |2\rangle$ transition at the crossover point. Since our system of equations represents two coupled optical transitions, each $S_{u\ell}(J)$ has four possible solutions, but real roots for only two. Each solution represents a different physical state of the system:

- (i) a solution for when both transitions are lasing (a real root for both S_{54} and S_{42});
- (ii) a solution for when transition $|5\rangle \rightarrow |4\rangle$ is lasing and transition $|4\rangle \rightarrow |2\rangle$ is not (a real root for only S_{54});
- (iii) a solution for when transition $|4\rangle \rightarrow |2\rangle$ is lasing and transition $|5\rangle \rightarrow |4\rangle$ is not (a real root for only S_{42});
- (iv) a solution for when neither transition is lasing (no real roots).

These solutions “cross” in temperature when transition $|5\rangle \rightarrow |4\rangle$ and transition $|4\rangle \rightarrow |2\rangle$ have the same threshold. Furthermore, each solution is only meaningful for a limited set of conditions. For example, at $T = 40$ K, we see four plotted values in Fig. 1.19, two for each optical transition. Of the two values that correspond to threshold for the $|5\rangle \rightarrow |4\rangle$ transition (red lines a and d), one value corresponds to when $|5\rangle \rightarrow |4\rangle$ is on and $|4\rangle \rightarrow |2\rangle$ is off, and the other corresponds to when both $|5\rangle \rightarrow |4\rangle$ and $|4\rangle \rightarrow |2\rangle$ are on. Since the values for the $|4\rangle \rightarrow |2\rangle$ transition (blue lines b and c) are both larger than the values for the $|5\rangle \rightarrow |4\rangle$ transition, the $|5\rangle \rightarrow |4\rangle$ threshold is less than the $|4\rangle \rightarrow |2\rangle$ threshold. Thus, the physically meaningful solutions at $T = 40$ K are represented by lines a and c .

With this understanding of the rate equation model, it is now easier to identify the origin of some of the unique threshold behavior features. While an increased LO phonon transition rate partially contributes to the rapid improvement in the $|4\rangle \rightarrow |2\rangle$ threshold

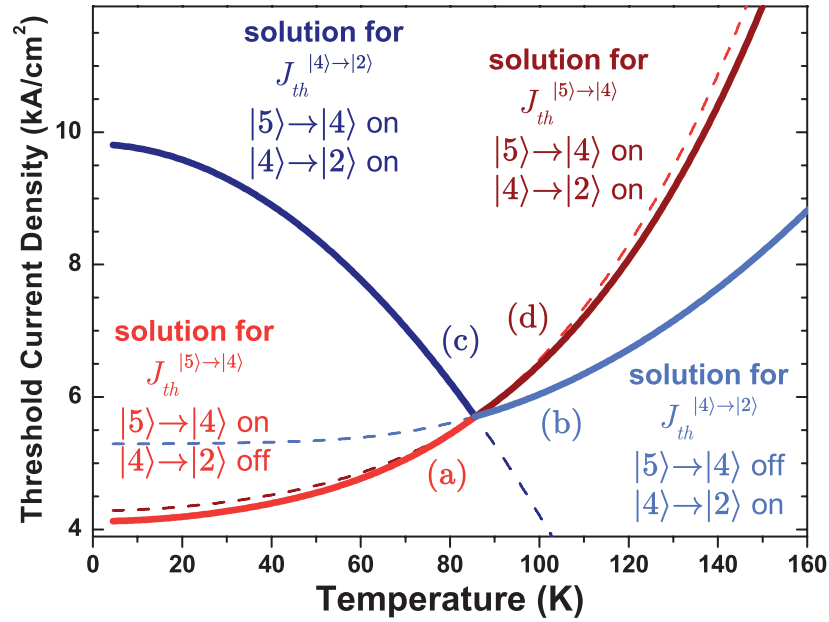


Figure 1.19: Model results for transition thresholds. Modeled temperature-dependent threshold current densities for the two optical transitions. Four solutions exist for each $S_{th}(T)$; only two are physically meaningful. The physically meaningful solutions correspond to (i) when a single transition reaches threshold and (ii) when both transitions have reached threshold. The physically meaningful portions of the solutions are plotted in bold lines.

around 55–85 K, the improvement is more aptly recast as a degradation in the $|5\rangle \rightarrow |4\rangle$ threshold, reflecting the fact that, when transition $|5\rangle \rightarrow |4\rangle$ is lasing, the $|4\rangle \rightarrow |2\rangle$ path is carrier-starved. The kink at the threshold crossover results from a transition between two different operating regimes of the laser: the regime where $|5\rangle \rightarrow |4\rangle$ has a lower threshold and the regime where $|4\rangle \rightarrow |2\rangle$ has a lower threshold.

1.8.3 Cavity-length-dependence of Threshold Crossover

The extremely low loss associated with the $|4\rangle \rightarrow |2\rangle$ transition results in a marked length-dependence of the two transition thresholds. As in a typical QC laser, the $|5\rangle \rightarrow |4\rangle$ loss is dominated by waveguide loss for most cavity lengths; mirror loss and waveguide loss are comparable for only very short cavity lengths (≤ 1 mm). In contrast, the $|4\rangle \rightarrow |2\rangle$ k -space transition total loss is dominated by mirror loss for even very large cavity lengths. Thus, since $\alpha_m = -\frac{1}{L} \ln(R)$, thresholds current densities decrease substantially faster with cavity length for transition $|4\rangle \rightarrow |2\rangle$ than they do for transition $|5\rangle \rightarrow |4\rangle$. The

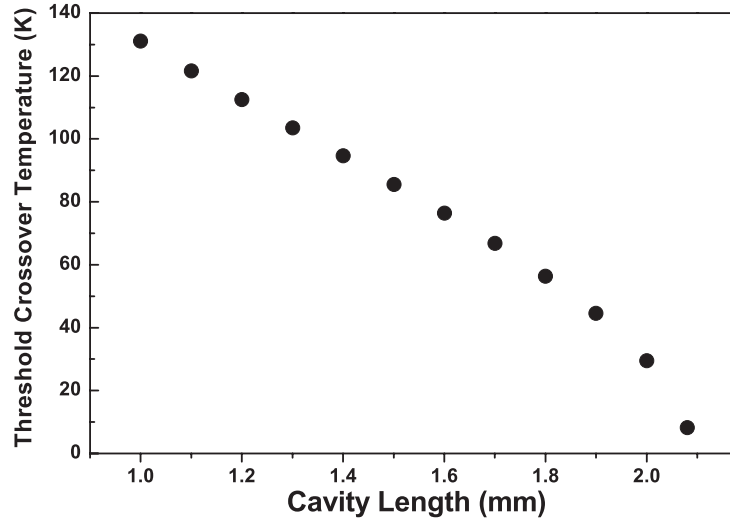


Figure 1.20: Cavity length dependence of transition threshold crossover temperature. Resulting from the extremely low optical loss of the $|4\rangle \rightarrow |2\rangle$ transition, the temperature at which the two transition thresholds cross is highly dependent on cavity length. Here, the rate equation model results are shown. Laser data confirm this behavior.

result is especially noticeable in temperature at which the threshold crossover occurs. Figure 1.20 plots calculated threshold crossover vs. cavity length, and we can see that, because the net gain increases with increasing cavity length for $|4\rangle \rightarrow |2\rangle$, the crossover temperature decreases with increasing cavity length.

1.9 Conclusions & Future Directions

1.9.1 Summary

The work presented in this chapter began with the investigation of a novel QC architecture: the use of an excited state lasing transition. Because of the extreme flexibility afforded by the general QC concept, unique designs that radically depart from the conventional QC configuration are relatively simple to implement. However, it is this exact same flexibility to innovate that led us to the primary result of this work so far. By injecting into an excited state optical transition, other lower-lying transitions also with large oscillator strengths were present in the active region; indeed, we confirmed lasing from such a lower-lying transition. Because of the unique configuration of our particular

laser design, population inversion was not achieved at the Γ point in the band structure for the lower transition. But, because electrons were injected via LO phonon scattering into a high k -space position, local population inversion high in k -space resulted in high k -space laser action. While both transitions lase simultaneously under certain conditions, the high k -space transition is anti-correlated with the primary, excited state laser transition. A rate equation model based on incorporating a high k -space optical transition reproduces the characteristic features of the observed temperature-dependent emission behavior.

To be sure, the demonstration of high k -space lasing represents a departure from the conventional approaches to semiconductor lasers. In semiconductor lasers, because of charge carriers' propensity for extremely fast momentum relaxation [29] [19], they accumulate at band extrema—i.e., near $k = 0$ in direct-gap semiconductors. Conventional wisdom thus holds that the “interesting” device-level physics happens at these band extrema, including population inversion for lasing. This behavior is universal among diode lasers [30] [31], interband quantum well lasers [32], and QC lasers.

The history of QC lasers is decorated with unique methods for obtaining laser action. Laser transitions with one state being a virtual state have been demonstrated both through Bloch gain [33] [34] and stimulated Raman scattering [35]. In every semiconductor injection mechanism to date though, inversion is achieved from electron populations in quasi-equilibrium and thermally distributed around the Γ -point. Our finding of k -space injection via LO phonons adds yet another fundamentally unique mechanism to the list of QC-based innovations.

In studying high k -space laser transitions, one cannot help but draw a parallel to the hot-hole (p-Ge) laser [36] [37]. Here, a combination of large crossed electric and magnetic fields preferentially populates the light hole band of a bulk semiconductor by trapping electrons in cyclotron orbits at high k -space, while the applied electric field sweeps holes out of the heavy hole band through streaming motion [38]. Once these streaming holes in the heavy hole band reach the energy of an optical phonon, a scattering path opens where they can then repopulate the light hole band. In the work presented here, instead of using externally applied electric and magnetic fields, we employ the optical phonons, a process intrinsic to the material.

1.9.2 Future Direction: *Intentionally* create k -space lasers

The possibility of designing intersubband devices that make more cognizant use of full k -space population distributions provides a variety of intriguing advantages and possible applications. The decoupling in energy of the optical emission and reabsorption processes is one point on which high k -space transitions are fundamentally superior to Γ -point transitions. It is certainly possible that high k -space transitions will one day lead to higher performing QC lasers. But other means may exist to capitalize on the high k -space concept.

In addition to the decoupling of emission and absorption, another interesting result of the built-in non-parabolicity is the range over which the transition “tunes” as it moves in k -space. If one can make a global population inversion for subbands that are pumped at high k -space, an additional method for creating tunable QC lasers could be realized. Today’s most tunable QC sources rely on broadening the gain spectrum by a number of means: rough interfaces [10], bound-to-continuum designs [39], diagonal transitions [40], etc. Placed in an external cavity setup [41] or a DFB array [42], these methods can yield tunability in the range of 100 cm^{-1} . In comparison, the non-optimized k -space transition in our laser had a tuning range in k -space of about 16 meV, or 130 cm^{-1} . Coupling a high k -space transition with other broadening mechanisms could ultimately yield much better spectral coverage out of a single laser device.

Extension of the k -space concept need not be strictly limited to QC lasers. Our demonstration of the usefulness of electrons in highly non-equilibrium states could be useful in other semiconductor and opto-electronic devices and systems. For example, in indirect bandgap semiconductors such as silicon, achieving laser action through the traditional across-gap mechanism has proven elusive. The ability to use non-equilibrium electrons, e.g. populating a “state” at the Γ -point, could expose new possible routes to achieving lasing in these systems.

Before exploring the strategic use of high k -space transitions, one must confront and resolve a primary challenge: how best to populate the high k -space state? We have demonstrated that the momentum transfer associated with LO phonons can accomplish the task; Yamanishi *et al.* have demonstrated a similar upper laser state population mechanism [43]. However, using the electron-LO phonon process may ultimately prove to be a transport bottleneck that limits performance [40]. Another possibility might be

taking advantage of the (normally) parasitic satellite k -space valleys. Given sufficient electron energy above the band edge, electron-electron scattering between valleys is extremely rapid. Innovation on this front will be necessary to realize a practical high k -space device.

1.9.3 Future Direction: Further develop the excited state concept

The work on QC lasers specifically designed to maximize the large oscillator strengths accompanying excited state transitions is ongoing. Whether this design strategy will ultimately be useful for long-wavelength lasing remains to be proven. As demonstrated throughout the chapter, achieving high performance at long-wavelengths is hindered by multiple challenges. While the excited state strategy addresses some of these challenges by compensating for large optical losses with larger oscillator strengths, the strategy itself introduces some new challenges. For example, excited state transitions can make achieving population inversion even more difficult. When more lower states are added below the optical transition, as in excited state structures, the ratio $\left(1 - \frac{\tau_\ell}{\tau_{u\ell}}\right)$ gets smaller. A carefully balanced design will ultimately yield the best trade-off between this effect of decreased lifetimes and maximizing oscillator strength.

Another primary challenge for the excited state strategy that must be overcome is the huge energy drop between optical transitions, the effective Δ_{inj} . While such a large Δ_{inj} can aggravate the problem of resonant absorption in the injector region, it also leads to a significant reduction in wall-plug efficiency. Careful design can minimize injector region resonant absorption. A potential fix for the hit to wall-plug efficiency might be engineering two optical transitions of the same energy in the active region. By creating a “double photon” structure, energy that would normally be surrendered to the lattice can be used to create more photons.

1.9.4 Future Direction: Correlated photons

In this chapter, we have shown that simultaneous lasing is in principle possible from stacked transitions. In the QC design and devices presented here, the lower optical transition did not achieve population inversion at the Γ point due to a lack of states into which electrons could scatter. However, more careful design that specifically

seeks to empty out the lowest active region state could create an active region with stacked transitions that both attain population inversion at the Γ point. In this case, simultaneous lasing could lead to the generation of correlated photons.

One primary challenge of generating correlated photons by this strategy will be to maximize the transport path where electrons make two successive Γ -point optical transitions. Another transport path, where electrons scatter to the middle state of the stacked transitions via LO phonons, should be minimized. This favored setup, however, could in fact be a natural state of the system, since non-parabolicity will lead to different lasing energies for the lower transition of the two transport paths.

References

- [1] , “Uranium Enrichment,” *United States Nuclear Regulatory Commission*
- [2] P. Rabinowitz, A. Kaldor, A. Gnauck, R. L. Woodin, and J. S. Gethner, “Two-color infrared isotopically selective decomposition of UF_6 ,” *Opt. Lett.* **7**, 212 (1982).
doi:[10.1364/OL.7.000212](https://doi.org/10.1364/OL.7.000212)
- [3] Y. Okada, S. Tanimura, H. Okamura, A. Suda, H. Tashiro, and K. Takeuchi, “Vibrational spectroscopy and predissociation of UF_6 clusters in a supersonic Laval nozzle,” **410-411**, 299 (1997).
doi:[10.1016/S0022-2860\(96\)09567-1](https://doi.org/10.1016/S0022-2860(96)09567-1) Molecular Spectroscopy and Molecular Structure 1996
- [4] C. Gmachl, F. Capasso, A. Tredicucci, D. Sivco, A. Hutchinson, and A. Cho, “Long wavelength $\lambda \simeq 13 \mu\text{m}$ quantum cascade lasers,” **34**, 1103 (1998).
- [5] A. Tredicucci, C. Gmachl, F. Capasso, D. L. Sivco, A. L. Hutchinson, and A. Y. Cho, “Long wavelength superlattice quantum cascade lasers at $\lambda \simeq 17 \mu\text{m}$,” *Appl. Phys. Lett.* **74**, 638 (1999).
doi:[10.1063/1.123026](https://doi.org/10.1063/1.123026)
- [6] A. Tredicucci, C. Gmachl, M. C. Wanke, F. Capasso, A. L. Hutchinson, D. L. Sivco, S.-N. G. Chu, and A. Y. Cho, “Surface plasmon quantum cascade lasers at $\lambda \sim 19 \mu\text{m}$,” *Appl. Phys. Lett.* **77**, 2286 (2000).
doi:[10.1063/1.1316768](https://doi.org/10.1063/1.1316768)
- [7] R. Colombelli, F. Capasso, C. Gmachl, A. L. Hutchinson, D. L. Sivco, A. Tredicucci, M. C. Wanke, A. M. Sergent, and A. Y. Cho, “Far-infrared surface-plasmon quantum-cascade lasers at $21.5 \mu\text{m}$ and $24 \mu\text{m}$ wavelengths,” *Appl. Phys. Lett.* **78**, 2620 (2001).
doi:[10.1063/1.1367304](https://doi.org/10.1063/1.1367304)

- [8] M. Rochat, D. Hofstetter, M. Beck, and J. Faist, “Long-wavelength ($\lambda \approx 16 \mu\text{m}$), room-temperature, single-frequency quantum-cascade lasers based on a bound-to-continuum transition,” *Appl. Phys. Lett.* **79**, 4271 (2001).
doi:[10.1063/1.1425468](https://doi.org/10.1063/1.1425468)
- [9] A. A. Kosterev, R. F. Curl, F. K. Tittel, M. Rochat, D. Hofstetter, and J. Faist, “Chemical sensing with pulsed QC-DFB lasers operating at $15.6 \mu\text{m}$,” **75**, 351 (2002).
doi:[10.1007/s00340-002-0963-z](https://doi.org/10.1007/s00340-002-0963-z)
- [10] S. Tsujino, A. Borak, E. Müller, M. Scheinert, C. V. Falub, H. Sigg, D. Grützmacher, M. Giovannini, and J. Faist, “Interface-roughness-induced broadening of inter-subband electroluminescence in p-SiGe and n-GaInAs/AlInAs quantum-cascade structures,” *Appl. Phys. Lett.* **86**, 062113 (2005).
doi:[10.1063/1.1862344](https://doi.org/10.1063/1.1862344)
- [11] M. Beck, D. Hofstetter, T. Aellen, J. Faist, U. Oesterle, M. Illegems, E. Gini, and H. Melchior, “Continuous Wave Operation of a Mid-Infrared Semiconductor Laser at Room Temperature,” *Science* **295**, 301 (2002).
- [12] M. O. Scully and M. S. Zubairy *Quantum Optics* Cambridge Univ. Press, New York (1997).
ISBN [0-521-43595-1](https://doi.org/10.1017/CBO9780511524444)
- [13] C. Sirtori, A. Tredicucci, F. Capasso, J. Faist, D. L. Sivco, A. L. Hutchinson, and A. Y. Cho, “Dual-wavelength emission from optically cascaded intersubband transitions,” *Opt. Lett.* **23**, 463 (1998).
doi:[10.1364/OL.23.000463](https://doi.org/10.1364/OL.23.000463)
- [14] S. S. Howard, Z. Liu, and C. F. Gmachl, “Thermal and stark-effect roll-over of quantum-cascade lasers,” *IEEE J. Quantum Electron.* **44**, 319 (2008).
doi:[10.1109/JQE.2007.912477](https://doi.org/10.1109/JQE.2007.912477)
- [15] J. Faist, F. Capasso, C. Sirtori, D. L. Sivco, A. L. Hutchinson, M. S. Hybertsen, and A. Y. Cho, “Quantum Cascade Lasers without Intersubband Population Inversion,” *Phys. Rev. Lett.* **76**, 411 (1996).
doi:[10.1103/PhysRevLett.76.411](https://doi.org/10.1103/PhysRevLett.76.411)

- [16] D. F. Nelson, R. C. Miller, and D. A. Kleinman, “Band nonparabolicity effects in semiconductor quantum wells,” *Phys. Rev. B* **35**, 7770 (1987).
doi:[10.1103/PhysRevB.35.7770](https://doi.org/10.1103/PhysRevB.35.7770)
- [17] C. Sirtori, F. Capasso, J. Faist, and S. Scandolo, “Nonparabolicity and a sum rule associated with bound-to-bound and bound-to-continuum intersubband transitions in quantum wells,” *Phys. Rev. B* **50**, 8663 (1994).
doi:[10.1103/PhysRevB.50.8663](https://doi.org/10.1103/PhysRevB.50.8663)
- [18] G. B. Serapiglia, K. L. Vodopyanov, and C. C. Phillips, “Nonequilibrium electron distributions in a three-subband InGaAs/InAlAs quantum well studied via double resonance spectroscopy,” *Appl. Phys. Lett.* **77**, 857 (2000).
doi:[10.1063/1.1306651](https://doi.org/10.1063/1.1306651)
- [19] A. M. Alcalde and G. Weber, “Nonparabolicity effects on electron–optical-phonon scattering rates in quantum wells,” *Phys. Rev. B* **56**, 9619 (1997).
doi:[10.1103/PhysRevB.56.9619](https://doi.org/10.1103/PhysRevB.56.9619)
- [20] B. K. Ridley *Quantum Processes in Semiconductors* Oxford Univ. Press 4th edn. (1999).
ISBN [0-19-850-580-9](https://doi.org/10.1017/CBO9780511524444)
- [21] S. Sinning, T. Dekorsy, M. Helm, G. Mussler, L. Däweritz, and K. H. Ploog, “Reduced subpicosecond electron relaxation in $\text{GaN}_x\text{As}_{1-x}$,” *Appl. Phys. Lett.* **86**, 161912 (2005).
doi:[10.1063/1.1904709](https://doi.org/10.1063/1.1904709)
- [22] P. Harrison *Quantum Wells, Wires and Dots: Theoretical and Computational Physics of Semiconductor Nanostructures* Wiley 2nd edn. (2005).
ISBN [0-470-01080-0](https://doi.org/10.1002/9780470010800)
- [23] U. Bockelmann and G. Bastard, “Phonon scattering and energy relaxation in two-, one-, and zero-dimensional electron gases,” *Phys. Rev. B* **42**, 8947 (1990).
doi:[10.1103/PhysRevB.42.8947](https://doi.org/10.1103/PhysRevB.42.8947)
- [24] V. Gorfinkel, S. Luryi, and B. Gelmont, “Theory of gain spectra for quantum cascade lasers and temperature dependence of their characteristics at low and moderate

- carrier concentrations,” *IEEE J. Quantum Electron.* **32**, 1995 (1996).
doi:[10.1109/3.541687](https://doi.org/10.1109/3.541687)
- [25] C. Gmachl, F. Capasso, D. L. Sivco, and A. Y. Cho, “Recent progress in quantum cascade lasers and applications,” **64**, 1533 (2001).
doi:[10.1088/0034-4885/64/11/204](https://doi.org/10.1088/0034-4885/64/11/204)
- [26] S. M. Sze *Physics of Semiconductor Devices* Wiley 2nd edn. (1981).
ISBN [0-471-05661-8](https://doi.org/10.1002/9780471056618)
- [27] J. Faist “,” In “,” (edited by H. C. Liu and F. Capasso) Semiconductors and Semimetals. Academic Press
- [28] Z. Liu, C. Gmachl, L. Cheng, F.-S. Choa, F. Towner, X. Wang, and J. Fan, “Temperature Dependence of Optical Gain and Loss in $\lambda \approx 8.2\text{--}10.2\text{ }\mu\text{m}$ Quantum-Cascade Lasers,” *IEEE J. Quantum Electron.* **44**, 485 (2008).
doi:[10.1109/JQE.2008.917273](https://doi.org/10.1109/JQE.2008.917273)
- [29] S. Rudin and T. L. Reinecke, “Electron–LO-phonon scattering rates in semiconductor quantum wells,” *Phys. Rev. B* **41**, 7713 (1990).
doi:[10.1103/PhysRevB.41.7713](https://doi.org/10.1103/PhysRevB.41.7713)
- [30] Z. I. Alferov, “The double heterostructure concept and its applications in physics, electronics, and technology,” *Rev. Mod. Phys.* **73**, 767 (2001).
doi:[10.1103/RevModPhys.73.767](https://doi.org/10.1103/RevModPhys.73.767)
- [31] H. Kroemer, “Quasielectric fields and band offsets: teaching electrons new tricks,” *Rev. Mod. Phys.* **73**, 783 (2001).
doi:[10.1103/RevModPhys.73.783](https://doi.org/10.1103/RevModPhys.73.783)
- [32] L. J. Olafsen, I. Vurgaftman, and J. R. Meyer “Antimonide Mid-IR Lasers,” In “Long-wavelength Infrared Semiconductor Lasers,” (edited by H. K. Choi). Wiley (2004).
- [33] R. Terazzi, T. Gresch, M. Giovannini, N. Hoyler, N. Sekine, and J. Faist, “Bloch gain in quantum cascade lasers,” **3**, 329 (2007).
doi:[10.1038/nphys577](https://doi.org/10.1038/nphys577) Terazzi, Romain Gresch, Tobias Giovannini, Marcella Hoyler, Nicolas Sekine, Norihiko Faist, Jerome

- [34] D. G. Revin, M. R. Soulby, J. W. Cockburn, Q. Yang, C. Manz, and J. Wagner, "Dispersive gain and loss in midinfrared quantum cascade laser," *Appl. Phys. Lett.* **92**, 081110 (2008).
doi:[10.1063/1.2884699](https://doi.org/10.1063/1.2884699)
- [35] M. Troccoli, A. Belyanin, F. Capasso, E. Cubukcu, D. L. Sivco, and A. Y. Cho, "Raman injection laser," *Nature* **433**, 845 (2005).
doi:[10.1038/nature03330](https://doi.org/10.1038/nature03330)
- [36] V. Shastin, "Hot hole inter-sub-band transition p-Ge FIR laser," *Opt. Quantum Electron.* **23**, S111 (1991).
doi:[10.1007/BF00619761](https://doi.org/10.1007/BF00619761)
- [37] E. Br undermann "Widely Tunable Far-Infrared Hot-Hole Semiconductor Lasers," In "Long-wavelength Infrared Semiconductor Lasers," (edited by H. K. Choi). Wiley (2004).
- [38] W. E. Pinson and R. Bray, "Experimental Determination of the Energy Distribution Functions and Analysis of the Energy-Loss Mechanisms of Hot Carriers in *p*-Type Germanium," *Phys. Rev.* **136**, A1449 (1964).
doi:[10.1103/PhysRev.136.A1449](https://doi.org/10.1103/PhysRev.136.A1449)
- [39] A. Wittmann, T. Gresch, E. Gini, L. Hvozdar, N. Hoyler, M. Giovannini, and J. Faist, "High-Performance Bound-to-Continuum Quantum-Cascade Lasers for Broad-Gain Applications," *Quantum Electronics, IEEE Journal of* **44**, 36 (2008).
doi:[10.1109/JQE.2007.909516](https://doi.org/10.1109/JQE.2007.909516)
- [40] Y. Yao, Z. Liu, A. J. Hoffman, K. J. Franz, and C. F. Gmachl, "Voltage Tunability of Quantum Cascade Lasers," *IEEE J. Quantum Electron.* (2009).
- [41] G. Wysocki, R. Lewicki, R. F. Curl, F. K. Tittel, L. Diehl, F. Capasso, M. Troccoli, G. Hofler, D. Bour, S. Corzine, R. Maulini, M. Giovannini, and J. Faist, "Widely tunable mode-hop free external cavity quantum cascade lasers for high resolution spectroscopy and chemical sensing," **92**, 305 (2008).
doi:[10.1007/s00340-008-3047-x](https://doi.org/10.1007/s00340-008-3047-x)

- [42] B. G. Lee, M. A. Belkin, R. Audet, J. MacArthur, L. Diehl, C. Pflügl, F. Capasso, D. C. Oakley, D. Chapman, A. Napoleone, D. Bour, S. Corzine, G. Höfler, and J. Faist, “Widely tunable single-mode quantum cascade laser source for mid-infrared spectroscopy,” *Appl. Phys. Lett.* **91**, 231101 (2007).
doi:[10.1063/1.2816909](https://doi.org/10.1063/1.2816909)
- [43] M. Yamanishi, K. Fujita, T. Edamura, and H. Kan, “Indirect pump scheme for quantum cascade lasers: dynamics of electron-transport and very high T_0 -values,” *Opt. Express* **16**, 20748 (2008).
doi:[10.1364/OE.16.020748](https://doi.org/10.1364/OE.16.020748)